Master Thesis

$NaYF_4:Er^{3+}/Yb^{3+}$ nanocrystals for nanothermometry

Exploring upconversion in $NaYF_4:Er^{3+}/Yb^{3+}$ nanocrystals for nanothermometry with a wide temperature range

Paul Timotheüs Prins

Supervisors:
R.G. Geitenbeek, MSc.
Prof. dr. A. Meijerink

CONDENSED MATTER AND INTERFACES
DEBYE INSTITUTE FOR NANOMATERIALS SCIENCE
DEPARTMENT OF CHEMISTRY, UTRECHT UNIVERSITY
PRINCETONPLEIN 5, 3584 CC UTRECHT, THE NETHERLANDS

August, 2016

Summary

In this work the temperature dependent upconversion luminescence of NaYF$_4$:Yb^{3+}/Er^{3+} nanocrystals is characterized over a large temperature range, relevant for thermometry in chemical reactors. The temperature of the nanocrystals determines the intensity ratio between the two green emission lines of erbium from the ^{2}H$_{11/2}$ level centred at 520 nm and from the ^{4}S$_{3/2}$ level centred at 540 nm. To this end, the green luminescence of erbium is monitored for different temperatures. The green emission of erbium is visible upon infrared excitation of ytterbium at 980 nm and following energy transfer upconversion. To allow for practical application of NaYF$_4$: Yb^{3+}/Er^{3+} as nanothermometer, the scale of nanocrystal synthesis is increased by a factor of four compared to existing procedures. The resulting monodisperse NaYF$_4$ nanocrystals have a size of 22 nm (± 1 nm) and show temperature dependent upconversion luminescence up to 600 K. Above this temperature the NaYF$_4$ nanocrystals melt together and the luminescence drops. A silica shell of *ca.* 10 nm has been grown around the NaYF$_4$ nanocrystals to overcome this problem. The resulting NaYF$_4$@SiO$_2$ nanocrystals show temperature dependent luminescence up to 900 K. The intensity ratio between the ^{2}H$_{11/2}$ level and the ^{4}S$_{3/2}$ level changes from *ca.* 0.4 at 300 K to *ca.* 3 at 900 K. The temperature variations of the intensity ratio are identical for five consecutive cycles, showing that the durability of the NaYF$_4$@SiO$_2$ nanocrystals is high. The accuracy of the measurements is high, with standard deviations of 1 K and 5 K below and above 750 K. Our results show that NaYF$_4$:Yb^{3+}/Er^{3+} nanocrystals can be used as a non-invasive thermometer up to 900 K after encapsulation in a protective silica shell. The broad temperature range, temperature resolution, and durability make that this system can be used to measure temperature variations inside a chemical reactor.

Contents

1 Introduction

Over the last two decades research in the nanoregime has yielded new materials with even more new applications. The development of nanomaterials also makes new measurement methods with high spatial resolution possible. Spatial variations in temperature, sometimes on the sub-micrometre scale, affect various processes in biology, chemistry and physics. Consequently, nanothermometry is a very active field of research, trying to develop non-invasive, accurate thermometers for the nanoscale. Until now the focus in the field of nanothermometry is mostly on biological applications[1–3].

However, there are more applications for thermometers with submicron spatial resolution. There is a demand for more accurate non-invasive thermometers with higher spatial resolution, to be able to investigate heat transfer and temperature variations on the nanoscale.

A promising non-invasive thermometry method is based on luminescence. Luminescence thermometry exploits the temperature dependence of the luminescence of materials. The change of temperature can be measured by monitoring the spectral position, bandwidth, intensity, polarization, or lifetime of the emission[2]. This thermometry method is non-invasive because temperature reading is done from a distance by recording the emitted light and does not affect the investigated material.

The suitable materials for luminescence thermometry can be divided into three groups, colloidal quantum dots[4], organic dye molecules[5], and materials containing lanthanide ions[6–8]. Quantum dots and organic dyes are bright, but they are usually not stable at elevated temperatures[9]. Moreover, quantum dots often consist of toxic materials[10]. Luminescent lanthanide ions can be introduced in either organic or inorganic compounds. Organic hosts usually have limited photostability and the high-energy molecular vibration can quench the lanthanide luminescence[11]. Inorganic materials, on the other hand, exhibit better chemical stability and lower phonon energy, leading to less quenching[11]. Therefore, doped inorganic compounds, *i.e.* doped glasses and crystalline materials, are frequently used as luminescent thermometers[12]. However, bulk-size thermometers provide limited spatial resolution. To measure the temperature on the nanoscale, new temperature probes with nanometre size are required.

There are three parameters that define how accurate the temperature is measured, the spatial, temporal, and temperature resolutions. The spatial and temporal resolution depend on the optical set-up, *i.e.* spotsize and dwell time required for a good signal. The temperature resolution, also known as the sensitivity, depends on the observed change in luminescence versus temperature. The change in luminescence is most frequently observed by monitoring the intensity ratio from two thermally coupled states. Kusama et al. introduced this technique in 1976 by the name fluorescence intensity ratio, an internally referenced (ratiometric) method[13]. Two levels are thermally coupled if the energy difference between the two levels is so small, that the population ratio of the two levels depends on temperature. The practical advantages of this method are the simple set-up required, *i.e.* an excitation source with a detector, and the intensity ratio is not depending on concentration of luminescent centres or excitation power, *i.e.* does not requires an internal standard.

Most of the research for luminescence nanothermometers is done in biological systems, frequently using $NaYF_4$: Yb^{3+}/Er^{3+} nanocrystals[14,15]. Conveniently, these nanocrystals can be excited in the infrared, where scattering is weak, so light penetration can be deep and emit in the visible, where detectors are sensitive[16]. This type of luminescence is enabled by a process called energy transfer upconversion. In this system there is energy transfer from ytterbium to erbium[17]. The luminescence nanothermometers for biological systems are used to measure the temperature *in vivo*[6–8]. The spatial, temporal, and temperature resolutions are typically in the order of 10^{-1} µm, 10 µs and 10^{-2} K respectively[1], with a confined temperature range between 300-320 K.

There are, however, other applications possible for thermometers with a high spatial resolution, but with different temperature ranges. For example, monitoring temperature variations in chemical reactors can be of huge interest to improve the selectivity, efficiency, and rate of chemical reactions. Most chemical reactions have a thermally activated barrier and an Arrhenius type behaviour, resulting in a strong effect of temperature on the reaction rate and selectivity.[18]. Many common chemicals are synthesized on a large scale in industrial reactors, where the temperature distribution can be very inhomogeneous. This can result in a lower yield and undesired by-products. To measure the temperature variations in working reactors *in situ*, new techniques are required. Conventional techniques average the temperature distribution throughout the reactor, or are not able to penetrate the reaction mixture[19,20]. Moreover, many industrial catalysts are structured on multiple length scales ranging down to the nanoscale, far below the spatial resolution of existing thermometry techniques[18]. Existing nanothermometers for the biological systems cannot be directly applied to chemical reactors, because they have been tested on too narrow temperature range. However, it has been demonstrated that the couple Yb^{3+}/Er^{3+} can be used as a luminescent thermometry probe at least up to 900 K in a bulk-size powder[21].

In this work the temperature dependent upconversion luminescence of $NaYF_4$:Yb^{3+}/Er^{3+} nanocrystals is characterized over a large temperature range, relevant for thermometry in chemical reactors. The temperature of the nanocrystals determines the intensity ratio between the two green emission lines of erbium from the $^2H_{11/2}$ level centred at 520 nm and from the $^4S_{3/2}$ level centred at 540 nm. To this end, the green luminescence of erbium is monitored for different temperatures. The green emission of erbium is visible upon infrared excitation of ytterbium at 980 nm and following energy transfer upconversion. To allow for practical application of $NaYF_4$: Yb^{3+}/Er^{3+} as nanothermometer, the scale of nanocrystal synthesis is increased by a factor of four compared to existing procedures. The resulting monodisperse $NaYF_4$ nanocrystals have a size of 22 nm (± 1 nm) and show temperature dependent upconversion luminescence up to 600 K. Above this temperature the $NaYF_4$ nanocrystals melt together and the luminescence drops. A silica shell of *ca.* 10 nm has been grown around the $NaYF_4$ nanocrystals to overcome this problem. The resulting $NaYF_4$@SiO_2 nanocrystals show temperature dependent luminescence up to 900 K. The intensity ratio between the $^2H_{11/2}$ level and the $^4S_{3/2}$ level changes from *ca.* 0.4 at 300 K to *ca.* 3 at 900 K. The temperature variations of the intensity ratio are identical for five consecutive cycles, showing that the durability of the $NaYF_4$@SiO_2 nanocrystals is high. The accuracy of the measurements is high, with standard deviations of 1 K and 5 K below and above 750 K.

Our results show that $NaYF_4$:Yb^{3+}/Er^{3+} nanocrystals can be used as a non-invasive thermometer up to 900 K after encapsulation in a protective silica shell. The broad temperature range, temperature resolution, and durability make that this system can be used to measure temperature variations inside a chemical reactor.

2 Theoretical background

In this research sodium yttrium tetrafluoride ($NaYF_4$) nanocrystals are doped with the lanthanide ions erbium (Er^{3+}) and ytterbium (Yb^{3+}). The characteristic green f-f luminescence of erbium is visible upon infrared excitation of ytterbium and following energy transfer. The thermally coupled excited state levels of erbium show temperature dependent luminescence, which can be used for ratiometric thermometry.

2.1 Lanthanides and f-f transitions

Erbium and ytterbium are part of the lanthanide series, comprising fifteen metallic chemical elements with atomic numbers 57 through 71, respectively from lanthanum (La) through lutetium (Lu). Since scandium (Sc) and yttrium (Y) are chemically similar as the lanthanides, they are often collectively called the rare earth elements. Most of the lanthanides commonly occur with an oxidation state of 3+[22]. The electronic configuration of these lanthanides as trivalent cations is $[Ln^{3+}]$ = [Xe] $4f^n$, with n varying from 0 to 14 for La^{3+} to Lu^{3+}. Within these 4f-orbitals, electrons can redistribute themselves by interacting with light, known as intraconfigurational f-f transitions. Because of these transitions most lanthanide ions have characteristic absorption and emission lines in the ultraviolet, visible and/or near-infrared part of the spectrum.

One characteristic of the luminescence of lanthanides is narrow emission and excitation transitions. This is because the 4f electrons are well shielded from the surroundings by the completely filled 5s and 5p orbitals (Figure 1)[23]. As a consequence of their shielding from the surroundings, the ground and excited states are weakly influenced by vibrational levels. This is in contrast with f-d transitions which show large influence of the surroundings on the ground and excited sates. Observable by strong and broad emission and absorption bands with a large energy difference for f-d luminesce.

The partly filled f-shell gives a large amount of possibilities to distribute the electrons over the different f-orbitals. If only the kinetic energy of the 4f electrons and the interactions with the nucleus would be taken into account, all the levels would have the same energy (H_0). By columbic repulsion between the electrons themselves (H_C), the electronic configurations are no longer degenerated, resulting in different energy levels. These different energy levels have a well-defined total orbital angular momentum L as well as a well-defined total spin angular momentum S, which can be described as LS-terms, ^{2S+1}L. By spin-orbit coupling (H_{SO}) the levels split into J-multiplets by interaction of the spin angular momentum of an electron with its orbital angular momentum. These states are also well-defined, namely by the total angular momentum $J = L + S$, which gives $^{2S+1}L_J$. The levels are ($2J + 1$)-fold degenerate. The splitting of the levels is visualized in Figure 2[24]. These resulting levels are in close agreement with the Dieke diagram[25,26], shown in Figure 3. At last, the influence of the crystal field on the energy levels (H_F) has to be taken into account. This influence is depicted by the thickness of the lines. These sublevels that are created by splitting through the electric field in the crystal are called stark-levels.
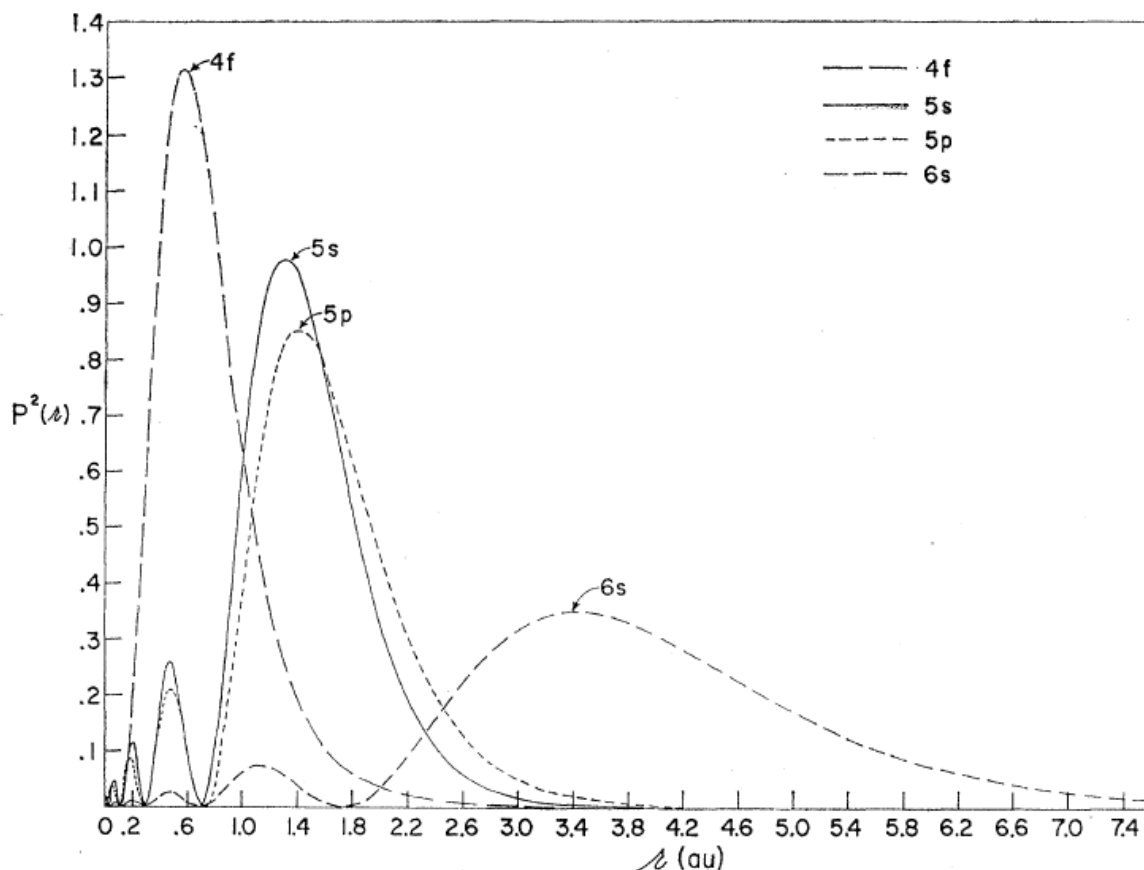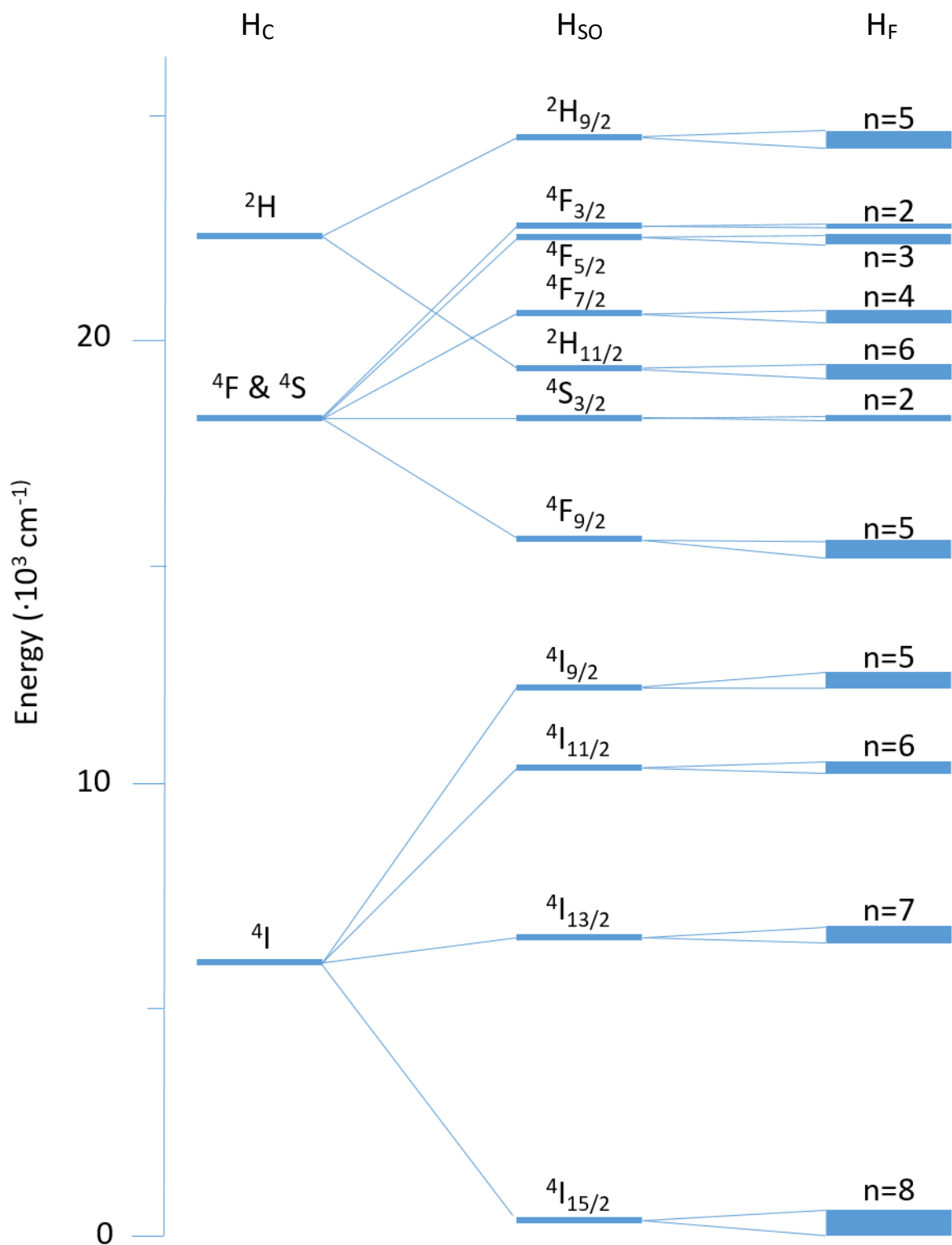
Figure 1 Square of the radial wavefunctions, *i.e.* probability to find an electron, for the 4f, 5s, 5p and 6s energy levels from Hartree-Fock. Calculated for the Gd^{3+} ion by Freeman and Watson[23].

A second characteristic of the luminescence of lanthanides is the low intensity of emission and excitation transitions. As mentioned before, the redistribution of electrons over the 4f-orbitals gives rise to the intraconfigurational f-f transitions. The Laporte selection rule dictates that transitions with the same parity are forbidden for centrosymmetric atoms because according to quantum mechanics, parity should be inverted during an electronic transition. All 4f states have odd parity ($l = 3$), so when the lanthanide ions have a centre of symmetry the f-f transitions are forbidden. However, the parity selection rule is relaxed for ions in a crystal which does not have perfect symmetry. Uneven crystal field components allow admixing with the opposite-parity 4f-5d transitions, known as forced electric dipole transitions. Hexagonal $NaYF_4$ has this preferred low inversion symmetry in the crystal field which promotes the excitation and emission of the erbium and ytterbium ions in the crystal[27].

Energy ($\cdot 10^3$ cm^{-1})

H_C H_{SO} H_F

$^2H_{9/2}$ n=5

^2H
$^4F_{3/2}$ n=2
$^4F_{5/2}$ n=3
$^4F_{7/2}$ n=4

20

^4F & ^4S
$^2H_{11/2}$ n=6
$^4S_{3/2}$ n=2

$^4F_{9/2}$ n=5

$^4I_{9/2}$ n=5

$^4I_{11/2}$ n=6

10

^4I
$^4I_{13/2}$ n=7

$^4I_{15/2}$ n=8

0

Figure 2 The 4f^{11}-configuration of Er^{3+} splits under influence of Coulomb interaction (H$_c$), spin-orbit coupling (H$_{SO}$), and the crystal field (H$_F$). The number of stark components (n) are given and the thickness of the lines represents the influence of the crystal field on the levels. The higher energy levels are not shown. Adapted from Kenyon[24].
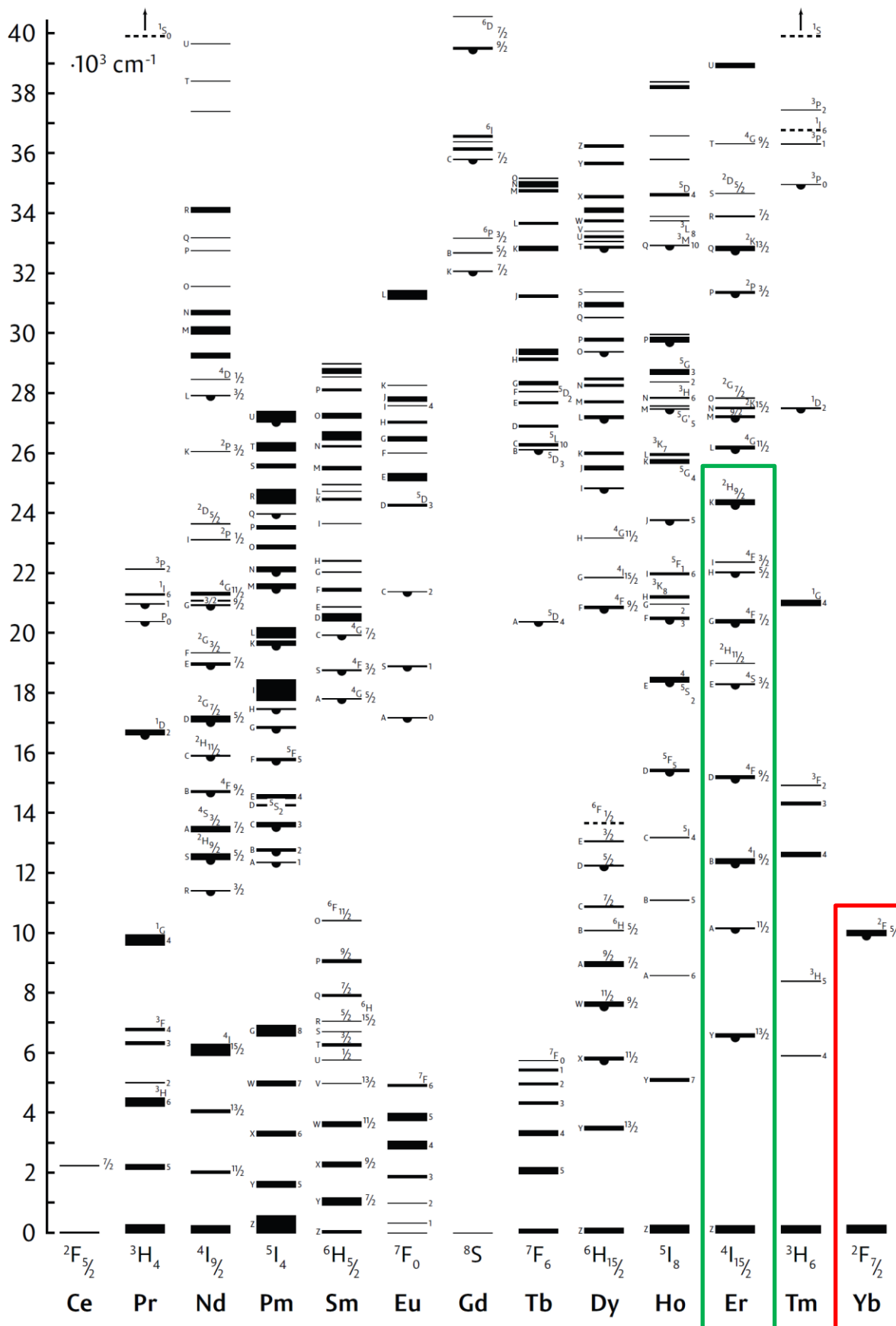
Figure 3 The Dieke diagram[25,26]; the green and red highlighted levels are relevant for this research. When comparing the green highlighted area with Figure 2, it can be noticed that they are in good accordance.

2.2 Decay of an excited state

After excitation of an erbium ion, the excited state can decay either radiatively or nonradiatively. The radiative decay rate of these excited states to the ground state is small (10^2-10^3 s^{-1})[11], because the transitions are parity forbidden/forced electric dipole transitions. Besides radiative decay (*r*), the excited states can nonradiatively (*nr*) decay (thermally) by using their energy to excite the surroundings or they can transfer their energy (*et*) to the surroundings, *e.g.* defects, ligands, solvents and neighbouring ions. The total decay rate (γ) is the sum of all these possibilities:

$$\gamma = \gamma_r + \gamma_{nr} + \gamma_{et}$$

The total decay rate can be determined by measuring the lifetime, as the lifetime τ is the inverse of the total decay rate $\tau = \frac{1}{\gamma}$. To prepare bright, luminescent nanocrystals, the γ_{nr} and γ_{et} to quenchers, should be minimised.

2.2.1 Multiphonon relaxation

Nonradiative rates (10^4 s^{-1})[11] exceed the radiative rates by a factor of (10^1-10^2 s^{-1}) and can dominate the total rate easily. Nonradiative decay in lanthanides is mostly caused by multiphonon relaxation[28], where energy is lost by exciting the vibrations in the host material. Multiphonon relaxation is significant, when the energy gap between the excited state and an underlying level is equal or less than 5 times the phonon energy in the host material, *i.e.* when it takes 5 or less phonons to bridge the energy gap. Multiphonon relaxation can be well-described by phonon statistics. The nonradiative multiphonon relaxation rate decreases exponentially with the number of phonons p. The number of phonons is given by, $p = \Delta E / \hbar\omega_{max}$, where ΔE is the energy gap, $\hbar\omega_{max}$ is the maximum phonon energy and ω_{max} is the maximum vibrational frequency of the phonons in the surroundings. In the case of NaYF$_4$ the maximum vibrational frequency of the lattice phonons is low (*ca.* 360 cm^{-1})[29], resulting in a small nonradiative decay rate. In contrast, organic frameworks have high frequency lattice vibrations (3000-3500 cm^{-1})[11], resulting in a large nonradiative decay rate. These vibrations are so high in energy that almost all of the higher energy gaps in the energy diagram from erbium are bridged by one or two phonons, resulting in low luminescence output. Therefore, these inorganic nanocrystals are used as host material and not organic frameworks.

2.3 Energy transfer

Before discussing the energy transfer to quenchers, the underlying theory of Förster resonance energy transfer[30] will be discussed. As stated earlier, an excited state, the donor, can transfer his energy to the surroundings, the acceptor. For energy transfer it is required that the emission spectrum of the donor (partially) overlaps with the absorption spectrum of the acceptor. The rate of energy transfer depends on the strength of the involved transitions (low for lanthanides since the f-f transitions are forbidden) and on the inverse sixth power of the donor-acceptor separation. The strength of energy transfer is frequently expressed as the critical Förster radius R_0. It is defined as the separation between donor and accepter, at which the energy transfer rate is equal to the intrinsic decay rate of the donor. The value for R_0 is typically in the order of a few ångströms for lanthanide donor/acceptor couples, but tens of ångströms for a lanthanide donor and an allowed transition acceptor. Because energy transfer strongly depends on the donor-accepter separation, it is very efficient at equal or smaller distances than R_0, but rapidly becomes negligible as the separation increases.

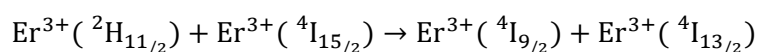### 2.3.1 Energy transfer to defects

When an excited state transfers its energy to a defect in the crystal, the energy will be lost as heat. To minimize the number of defects, well-defined crystalline nanocrystals should be grown in order to minimize loss processes via non-radiative processes. In nanocrystals an additional type of energy transfer to quenchers has to be taken into account, *i.e.* surface quenching. Comparing bulk to nanocrystals the surface-to-volume ratio is much higher for nanocrystals. Therefore, the ions on the surface have a non-negligible influence on the total rate. Erbium ions on the surface have a large

probability for nonradiative decay, because the ions can transfer energy to phonons of the high frequency vibrations in the ligand and/or the solvent molecules. Additionally, there are more defects, *i.e.* vacancies, at the surface which can act as quenchers. The vibrations and defects are allowed, broadband absorbers, resulting in a strong energy transfer process with a large R_0. As a consequence, the luminescence output of nanocrystals can be multiple orders of magnitude lower than for bulk. Often an insulating NaYF$_4$ shell without active ions is grown around the core particles, to prevent this type of quenching.

2.3.2 Energy migration

An excited state can transfer his energy either direct or indirect to a quencher, *e.g.* a defect in the crystal or vibration at the surface. This indirect energy transfer is possible because of energy migration over the lattice, by energy transfer to identical erbium ions. For this migration a certain concentration of erbium ions is required. As the emission and absorption are forbidden transitions, the energy transfer strength is expected to be low. However, the overlap is large because of the small stoke shift for lanthanides as discussed previously. Furthermore, the transfer rate[11] will easily surpass the radiative rate, 10^7 s^{-1} and 10^2-10^3 s^{-1} respectively. Consequently, the excitation energy can be transferred more than 10^4 times during the lifetime of the excited state. Thereby, the excitation energy can migrate far over the lattice, until it reaches a defect where the energy is lost nonradiatively. This phenomenon is called concentration quenching. At low concentrations this can be prevented because the average distance between erbium ions is larger than R_0, resulting in less efficient energy transfer between identical erbium ions, making it less likely that defects are reached.

Additional to concentration quenching, another quenching process occurs for erbium, *i.e.* cross-relaxation. The higher-energy level emission is quenched in favour of excitation of an erbium ion in the ground state. This process depends on the interaction between two erbium ions (Figure 4a).

$$\text{Er}^{3+}(\,^2\text{H}_{11/2}) + \text{Er}^{3+}(\,^4\text{I}_{15/2}) \rightarrow \text{Er}^{3+}(\,^4\text{I}_{9/2}) + \text{Er}^{3+}(\,^4\text{I}_{13/2})$$

These two types of quenching depend on the concentration of erbium ions. Therefore, the concentration is kept low for this research at 2%. Which is the optimal concentration according to the literature[29,31].
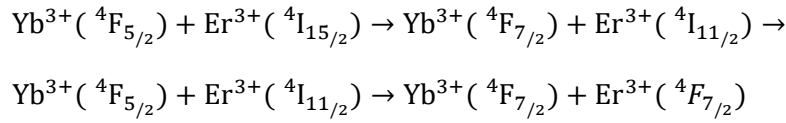
2.3.3 Energy transfer upconversion

A special case of energy transfer can occur between three ions, of which there are two ions in the excited state, the donors and one in the ground state, the acceptor. The two excited ions transfer their energy subsequently to the ion in the ground sate, the acceptor, which now can emit from a higher energy level (Figure 4c). This process is called energy transfer upconversion (ETU). Upconversion is also possible without energy transfer. In this case there is excited state absorption (ESA) within a single ion, *i.e.* two-step absorption (Figure 4b). Lanthanide ions make these processes possible because of the long lifetime of the excited states. However, the efficiencies of these two-photon upconversion processes are not high, 10^{-3} and 10^{-5} for ETU and ESA at 1 W cm^{-2} excitation power[17], respectively. This results in a low quantum yield for upconversion emission[32]. Because ETU and ESA are two-photon processes, the energy transfer efficiency depends quadratically on the excitation power.

Hexagonal NaYF$_4$ is the most used host material for upconversion. The hexagonal (β) phase exhibits an order of magnitude enhancement of the ETU efficiency relative to their cubic (α) phase counterparts[33] and an enhancement of forty times relative to other fluorides[11]. It is still unclear why β-NaYF$_4$ is the best material for ETU but it has something to do with the low inverse symmetry in the crystal lattice[27,34,35].

2.3.4 Energy transfer between different ions

For this research a double doped system is used, NaYF$_4$:Yb^{3+}/Er^{3+}. Additionally, to the energy transfer between identical ions, there is energy transfer between unlike ions. Ytterbium has a 10 times larger

absorption cross section $(11.7\cdot10^{-21}$ cm^2)[36] than erbium $(1.7\cdot10^{-21}$ cm^2)[36] and a large spectral overlap with the $^4I_{11/2}$ level from erbium (Figure 4c). This makes ytterbium the ideal ion for the ETU to erbium, increasing the luminescence output significantly. Especially since ETU is two-photon process and depends quadratically on the absorption, yielding an enhancement of 10^2.

$$Yb^{3+}(\,^4F_{5/2}) + Er^{3+}(\,^4I_{15/2}) \rightarrow Yb^{3+}(\,^4F_{7/2}) + Er^{3+}(\,^4I_{11/2}) \rightarrow$$

$$Yb^{3+}(\,^4F_{5/2}) + Er^{3+}(\,^4I_{11/2}) \rightarrow Yb^{3+}(\,^4F_{7/2}) + Er^{3+}(\,^4F_{7/2})$$

The ytterbium ions do not suffer from any kind of cross-relaxation quenching since they have just one excited state and concentration quenching only plays a significant role for concentrations above 15%. This is the reason that the optimal concentration of ytterbium is determined to be 18%[29,31]. If we combine this with the most ideal host material, hexagonal NaYF$_4$, and the optimal concentration for erbium, 2% as discussed earlier. This results in the β-NaYF$_4$:Yb^{3+}(18%)/Er^{3+}(2%) nanocrystals, used for this research.
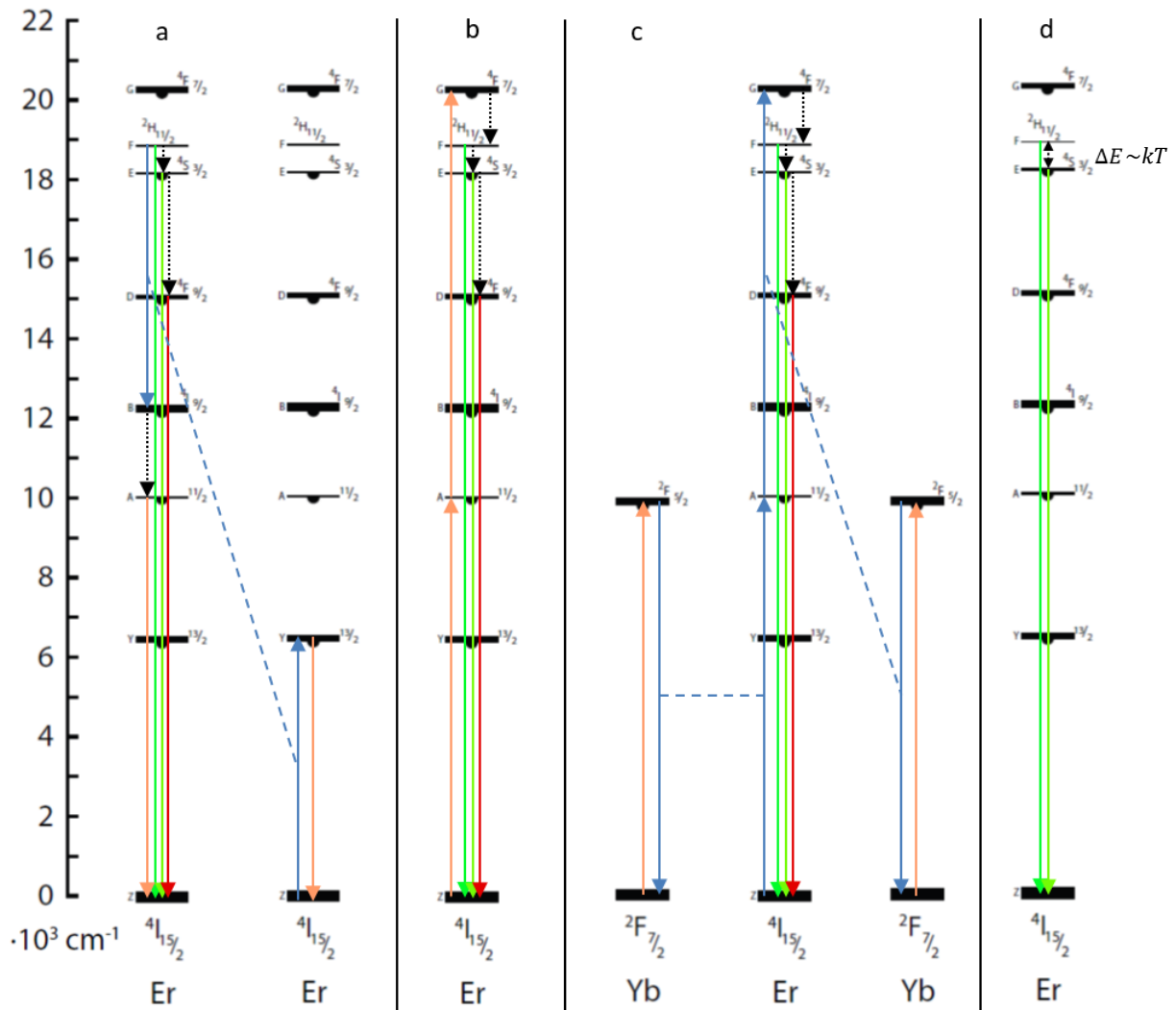
Figure 4 A simplified overview of some transitions in an erbium/ytterbium doped system. (a) Cross-relaxation energy transfer between two erbium ions competes with radiative decay from the $^2H_{11/2}$ level. (b) Excited state absorption upconversion within one erbium ion. (c) Energy transfer upconversion between two ytterbium ions and one erbium ion. (d) The $^2H_{11/2}$ level and the $^4S_{3/2}$ level are thermally coupled, because of the small energy difference between the two levels (ΔE). Green, red, and orange (IR) arrows represent excitation or emission. Black dotted arrows represent non-radiative decay. Blue arrows represent transitions involved with energy transfer visualized with a dashed blue line.

2.4 Thermally coupled states and FIR

The two excited states from the characteristic green luminescence, have a very small energy gap. Resulting in thermally coupled levels, ideal for fluorescence intensity ratio measurements to determine the temperature. In Figure 4d the energy scheme of erbium is shown to visualize the thermally coupled states.

2.4.1 Thermally coupled states

The energy gap between the $^2H_{11/2}$ level and the $^4S_{3/2}$ level is very small, 600 cm^{-1} according to the literature[35,29]. This is of the same order as the thermal energy at room temperature[37], $k_BT = 200$ cm^{-1}. Therefore, the two excited states will be in thermal equilibrium. Because the rate in which the equilibrium is set is on a picosecond timescale (10^{12} s^{-1})[38], it is dominant over the radiative, nonradiative and energy transfer rates.

2.4.2 FIR

From the ratio of the intensities of the transitions from the $^2H_{11/2}$ and the $^4S_{3/2}$ excited states to the $^4I_{15/2}$ ground state the temperature can be determined. The intensity of each transition is proportional to the total number of atoms in a given excited state, at temperature T (Equation 1). Where I_{ij} is the fluorescence intensity of the transition from the excited state energy level i to a ground state energy level j, g_i is the degeneracy of the excited state, σ_{ij} is the emission cross section between the upper and lower level, ω_{ij} is the angular frequency of the transition and N_i is the number of ions in the excited state.

$$I_{ij} = g_i \sigma_{ij} \omega_{ij} N_i \tag{1}$$

The relative population of these thermally coupled levels follows a Boltzmann type population[39], *i.e.* a quasi-equilibrium exists. The population of the higher $^2H_{11/2}$ level, $N_{^2H_{11/2}}$ is given in Equation 2 and depends on the population of the lower $^4S_{3/2}$ level, $N_{^4S_{3/2}}$ and the Boltzmann factor. Where ΔE is the energy gap between the levels (600 cm^{-1}), k_B is the Boltzmann constant[40] with a value of 0.695 cm^{-1}/K and T is the absolute temperature in K.

$$N_{^2H_{11/2}} = N_{^4S_{3/2}} e^{-\frac{\Delta E}{k_BT}} \tag{2}$$

For the experimental determination of the intensity ratio, two non-overlapping transitions with an energy separation comparable to the thermal energy are used. This results in the ratiometric (or self-referencing) measurement named FIR[12,41]. This technique can be taken as a measurement of absolute temperature, given that:

$$FIR = \frac{I_{^2H_{11/2} \to {^4I_{15/2}}}}{I_{^4S_{3/2} \to {^4I_{15/2}}}} = \frac{g_{^2H_{11/2}} \sigma_{^2H_{11/2} \to {^4I_{15/2}}} \omega_{^2H_{11/2} \to {^4I_{15/2}}}}{g_{^4S_{3/2}} \sigma_{^4S_{3/2} \to {^4I_{15/2}}} \omega_{^4S_{3/2} \to {^4I_{15/2}}}} e^{-\frac{\Delta E}{k_BT}} = B e^{-\frac{\Delta E}{k_BT}} \tag{3}$$

where B is a constant independent of T. When increasing the temperature, the population of the higher energy $^2H_{11/2}$ level increases relatively to the lower $^4S_{3/2}$ level. This seems logical because at higher temperature there is more thermal energy available to populate the higher energy level. One can derive from Equation 3, that the slope of the line will give the ΔE after being divided by $-k_B$.

The sensitivity is determined by the change in FIR with change in temperature[2,42]. To compare broad categories of temperature sensors, the sensitivity is normalized to have a relative sensitivity. The relative sensitivity (S) is also temperature dependent and defined by Equation 4.

$$S = \frac{1}{FIR}\frac{dFIR}{dT} = \frac{\Delta E_{21}}{k_B T^2}$$

(4)

Equation 4 suggests that when using pairs of energy levels with larger energy differences, the FIR sensitivity increases. While this is true to some extent, care needs to be taken that the levels are not too far apart, and thermalisation is no longer observed. Additionally, as the energy difference widens, the population and hence the fluorescence intensity from the upper thermalizing level will decrease, which may introduce practical problems in trying to measure very low light levels. The sensitivity is only a theoretical, internal sensitivity. Additional to the internal sensitivity, important contributions are made by how the measurements are physically performed, *i.e.* depends on the ability to detect temperature changes. For this reason, it is better to express the sensitivity as the error in the temperature measurement, *i.e.* the external sensitivity.

3 Methods

To allow for practical application of NaYF$_4$: Yb^{3+}/Er^{3+} as a nanothermometer, the scale of nanocrystal synthesis is increased by a factor of four compared to existing procedures. The NaYF$_4$ nanocrystals are synthesized by a co-precipitation method and the NaYF$_4$@SiO$_2$ nanocrystals are synthesized by a reverse micro-emulsion method.

3.1 Synthesis of NaYF$_4$ nanocrystals

There are multiple ways to synthesise nanocrystals doped with lanthanide-ions. The three most used ways are high temperature co-precipitation, thermal decomposition, and hydro(solvo)thermal synthesis. All methods can be used to synthesize high-quality lanthanide-doped luminescent nanocrystals featuring controlled morphology, well dispersibility, high crystallinity, and desirable optical properties.

Co-precipitation has no need for costly equipment, stringent reaction conditions, and complex procedures, resulting in less time consumption. Thermal decomposition is the decomposition of a metal trifluoroacetate precursor in the presence of oleic acid and octadecene. The nanocrystals synthesized with this method are of high quality and monodisperse but it requires expensive, air-sensitive metal precursors and produces toxic by-products[43]. Hydro(solvo)thermal synthesis requires cheap raw materials, no post-heat treatment and excellent control over particle size and shape. However specialized reaction vessels are required known as autoclaves, which does not give the possibility of observing the nanocrystals as it grows. The hydro(solvo)thermal synthesis utilizes a solvent under pressures and temperatures above its critical point, to increase the solubility of solids and to speed up reactions between solids[44]. All three syntheses are within the practical possibilities of synthesizing the particles for achieving the research goal. However, the co-precipitation method is used to synthesize the nanocrystals for this work because it is less time-consuming and it is the most user-friendly in contrast to hydro(solvo)thermal and thermal decomposition, respectively.

The NaYF$_4$:Er^{3+}/Yb^{3+} nanocrystals are synthesized through a co-precipitation method based on the work of Li and Zhang[45], with some adjustments based on the work of Wang and co-workers[46]. In this synthesis, 'the nucleation and growth' of the NaYF$_4$ nanocrystals are separated by carrying out the two stages respectively at low (20 °C) and elevated (300 °C) temperatures. The heating process controls in this way, the size of the particles by the height of the temperature. The nucleation and growth rates can be further controlled by adjusting the concentration of the precipitator, leading to largely tuneable particle sizes.

After adding the precipitators at low temperature (20 °C), the nucleation of cubic α-phase NaYF$_4$ particles takes place. Normally, when increasing the temperature, Ostwald-ripening leads to broadening of their particle size in the absence of additional monomer precursors. However, when heating is continued for sufficiently long time (110 minutes at 300 °C), small seeds of the hexagonal β-phase nucleate in solution. After nucleation of these seeds, the α-phase particles rapidly dissolve whereas the β-phase seeds rapidly increase in size. The fast release of monomers during the rapid dissolution of the α-phase, results in a monomer concentration so high that the particles of the less soluble β-phase grow under the condition of monomer supersaturation. This observation can be explained by a higher solubility of the thermodynamically less stable α-phase. The condition of monomer supersaturation can be maintained for rather long periods of time since the α-phase particles release new monomers as long as their particle size is smaller than the critical particle size under the given reaction conditions. Growth conditions where new monomer is constantly produced at high rate, result in strong focussing of the β-phase particle size distribution[47,48].

3.1.1 Synthesis protocol

The synthesis is performed in a Schlenk line to work under inert environment (N_2) or vacuum. During the complete reaction, the reactants are stirred vigorously to make sure that the heat and mass transfer flow is homogenous. First, 4 mmol of lanthanide triacetate ($Ln(Ac)_3$) with a Y:Yb:Er ratio of 80:18:2, is added to a mixture of 24 mL oleic acid (OA) and 68 mL 1-octadecene (ODE). The reaction mixture is degassed at 120 °C for 90 minutes to dissolve the lanthanide acetate salts and form the lanthanide-oleate precursor complexes and to remove water, acetic acid, and air. This results in a clear, slightly yellowish solution. To make sure there is (almost) no water or oxygen left, the mixture is flushed with N_2/vacuum thrice before cooling down to room temperature under a gentle flow of nitrogen.

The nucleation of the α-phase $NaYF_4$ particles is triggered by the injection of a methanol solution of the precipitators NaOH (10 mmol) and NH_4F (16 mmol) in respectively 10 and 28 mL. The precursors are mixed just before the addition to the reaction mixture. The combined use of NaOH and NH_4F enables a finer control over the reaction rate and when added quickly, it supresses the formation of unwanted NaF. The reaction is slow and when it is done overnight at room temperature, it results in monodisperse α-phase particles. Before the growth step the excess of methanol is removed by heating the reaction mixture to 100 °C under vacuum for 30 minutes. Afterwards the mixture was flushed thrice using N_2 and vacuum. As described previously, the dissolving of the α-phase particles is initiated by increasing the temperature to 300 °C. After keeping this temperature for 110 minutes it results in β-phase particles of 20-25 nm.

3.1.2 Washing protocol

After the synthesis, the reaction mixture is washed to remove excess reagents, solvents, and ligands. This is done by doubling the volume of the reaction mixture with ethanol, centrifuging at 2750 rpm for 8 minutes and removing the supernatant. The nanocrystals are redispersed in 12 mL cyclohexane and the washing is repeated twice. In the last washing step after redispersing the nanocrystals, an equal amount of oleic acid is added and the mixture is sonicated for 15 minutes. This turbid dispersion is than centrifuged and the nanocrystals are redispersed in 12 mL of cyclohexane again, resulting in a slightly turbid yellowish dispersion. The additional step with oleic acid is used to increase the ligand density and thus improve the colloidal stability. This is especially important for the silica coating of the nanocrystals.

A detailed step-by-step protocol as used for synthesizing the lanthanide doped $NaYF_4$ nanocrystals is available in Appendices A.

3.2 Silica coating of the NaYF₄ nanocrystals

The reverse micro-emulsion method used to grow the silica around the nanocrystals is found in literature[49]. The reaction mechanism of the synthesis is schematically illustrated in Figure 5. Again, the synthesis is done on a larger scale, 10 times larger than usually.

In short (step-by-step protocol in Appendices B), *ca.* 100 mg of NCs dispersed in cyclohexane is added to a mixture of 13 g NP-5 in 108 mL cyclohexane and stirred for at least 15 minutes. Next, 800 μL of TEOS and 1.5 mL of ammonium hydroxide is added to the mixture, while stirring for at least 15 minutes between additions. After the last addition, the sample is stirred for one minute and stored for *ca.* 24 hours.

Afterwards, the micelles are destroyed by addition of 30 mL of ethanol resulting in flocculation. Subsequently, the nanocrystals are separated of excess precursors, solvents and surfactants by centrifuging at 2750 rpm for 10 minutes. Subsequently, the nanocrystals are washed twice, by redispersing the nanocrystals in 100 mL of ethanol and then centrifuging at the same speed for 20 and 40 minutes. After the second time centrifuging, the particles are redispersed in 100 mL of ethanol. The obtained dispersion is slightly turbid.
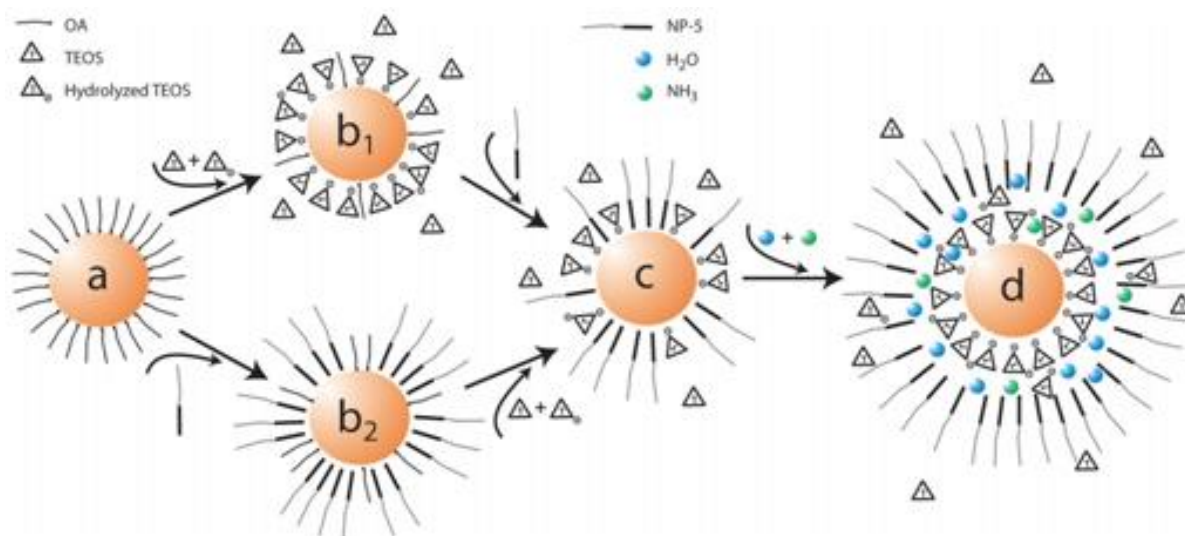
Figure 5 (a) Illustrates the OA coated nanocrystals dispersed in cyclohexane. Upon addition of TEOS or NP-5 the OA is largely replaced, resulting in TEOS (b_1) or NP-5 (b_2) coated nanocrystals. When subsequently NP-5 or TEOS is added, the same equilibrium is obtained (c), where the nanocrystals are coated by (hydrolysed) TEOS and NP-5. Upon addition of ammonia, TEOS is further hydrolysed, and replaces all NP-5 (d). Water and ammonia molecules are present in between the TEOS coated nanocrystal and the micelle that is formed by NP-5[49].

3.3 Setup and chemicals

Room temperature transmission electron microscopy (TEM) characterization was performed using a FEI Tecnai20F operating at 200 kV and a spotsize of 5. Energy dispersive X-ray spectroscopy (EDX) measurements took 3-5 minutes and were performed using an ultrathin window EDAX-detector and subsequently analysed using Tecnai Imaging and Analysis software.

Room temperature XRD measurements are carried out on a Bruker-AXS D2 Phaser powder X-ray diffractometer, in Bragg-Brentano mode, equipped with a Lynxeye detector. The working voltage, current and radiation source are 30 kV, 10 mA and Co Kα (λ = 1.79 Å) respectively.

Emission spectra and photoluminescence (PL) decay curves were recorded using an Edinburgh Instruments FLS920 spectrofluorometer equipped with a Hamamatsu R928 photomultiplier tube with a grating blazed at 500 nm. For upconversion emission spectra, a 980 nm 2W continuous wave laser was used for excitation in the $^2F_{5/2}$ level of Yb^{3+}. For PL decay measurements an optical parametric oscillator (OPO) system, Opotek He 355 II, was used, with a pulse width of 10 ns and a repetition rate of 20 Hz and pulse energy of *ca.* 3 mJ.

The temperature dependent measurements set-up is visualized in Appendices C. The temperature is controlled by a thermocouple, which corrects for all external heat, *e.g.* the 2W CW laser. The steps in temperature are 25 K, set to reach in one minute. The dwell time is investigated by taking measurements every five minutes starting at 1 minute after reaching the temperature set-point up to 16 minutes, *i.e.* fours measurements with steps of five minutes. The measurements show no trend over time, the error in the data is considered to be the measurement error only. The data presented in this work is measured five times per temperature set-point after a dwell time of 15 minutes.

All chemicals were used without further purification. The following chemicals were purchased from Sigma-Aldrich: Cyclohexane (99.5%, CH), oleic acid (90%, OA), 1-octadecene (90%, ODE), methanol (>99.85%, MeOH), sodium hydroxide (>97%, NaOH), ammonium fluoride (>98%, NH_4F), ammonium hydroxide (28% in H_2O, NH_3), lanthanide acetate hydrates (99.9%, $Ln(Ac)_3$), tetraethyl orthosilicate (99.999%, TEOS) and IGEPAL CO-520 (average Mn = 441 g mol^{-1}, NP-5). Ethanol (94-96%, EtOH) was purchased from Alfa Aesar.

4 Results

In this research the conventional protocols are improved to yield a larger number of particles by synthesizing on a four times larger scale. Additionally, the colloidal stability is increased by increasing the fraction of ligands on the surfaces of the nanocrystals. These two steps were required for a large scale production of the nanocrystals and the silica coating of the nanocrystals respectively.

After synthesizing the particles, the $NaYF_4$ nanocrystals and the $NaYF_4@SiO_2$ nanocrystals are characterized. First the structural characterization is done by TEM, EDX, and XRD, to verify that the nanocrystals are synthesized successful. Secondly, the luminescence properties where studied and thirdly how this luminescence depends on the temperature.

4.1 Upscaling and silica growth

The first step is synthesizing the nanocrystals at a larger scale than the conventional protocols. As a start the nanocrystals were synthesized on a small scale, the most occurring synthesis scale in literature[45,46]. Which is on a four times smaller scale than the scale described in the protocol. This resulted in monodisperse nanocrystals of 20-25 nm size. Subsequently, the synthesis was done on a four times larger scale with nucleation times of two hours and twelve hours.

In Figure 6 we show the nanocrystals synthesized with a nucleation time of two hours (a) and with a nucleation time of twelve hours (b). The nanocrystals in Figure 6a are polydisperse and seem to have two different size distributions of smaller (*ca.* 7 nm) and larger (*ca.* 22 nm) nanocrystals. The nanocrystals in Figure 6b are monodisperse and *ca.* 22 nm in size. The two different size distributions observed in Figure 6a are presumed to be α-phase particles and β-phase particles respectively. A hypothesis for these two distributions is that during nucleation not all of the monomer material is used to nucleate α-phase particles. While increasing the temperature for growing the nanocrystals, the α-phase particle increases in size because there are still monomers available in the reaction mixture. Resulting in α-phase particles with a size larger than the critical particle size at which they dissolve at 300 °C to subsequently form β-phase particles. When increasing the nucleation time to twelve hours all the monomer material is consumed, leaving no material available to grow for the α-phase particles when heating the reacting mixture. Consequently, the α-phase particles have a size smaller than the critical particles size at which they dissolve at 300 °C, initiating well-focused growth of β-phase particles. With this adjustment, the synthesis of monodisperse $NaYF_4$ nanocrystals at a four times larger scale was successful (Figure 6b).
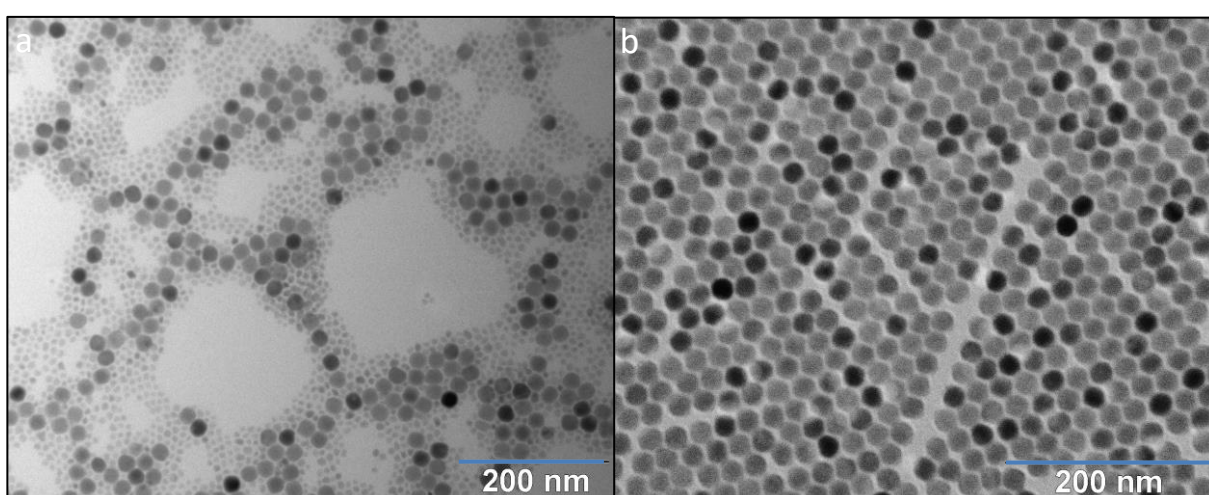
Figure 6 (a) TEM images of the polydisperse $NaYF_4$ nanocrystals synthesized with a nucleation time of two hours. (b) TEM images of the monodisperse $NaYF_4$ nanocrystals synthesized with a nucleation time of twelve hours.

The second step is coating the nanocrystals with silica. In Figure 7a and Figure 7c TEM images of the NaYF$_4$ nanocrystals are shown, respectively without and with an additional washing step with oleic acid (as described in 3.1.2). The additional washing step is added to increase the ligand density on the surface of the nanocrystals. The difference in ligand density is visible on TEM images by comparing the packing of the nanocrystals. These are respectively randomly and orderly packed for low (a) and high (c) ligand density. Figure 7b and Figure 7d show TEM images of silica coating of the NaYF$_4$ nanocrystals shown in Figure 7a and Figure 7b, respectively. The silica coating of the nanocrystals with the low ligand density resulted in clustering and encapsulation of multiple nanocrystals inside a single silica shell (d). Multiple nanocrystals inside a single silica shell is observed when the concentration of nanocrystals is too high[49], *i.e.* more nanocrystals than micelles. However, in Figure 7b there are also empty silica spheres visible, which excludes that explanation. On the other hand, the silica coating of the nanocrystals with high ligand density was successful.

Concluding, the colloidal stability of the NaYF$_4$ nanocrystals without additional ligands is too low resulting in clustering and encapsulation of multiple nanocrystals inside a single silica shell. This problem is solved by adding an additional washing step with oleic acid to increase the ligand density and consequently the colloidal stability, resulting in encapsulating single NaYF$_4$ nanocrystals with silica.
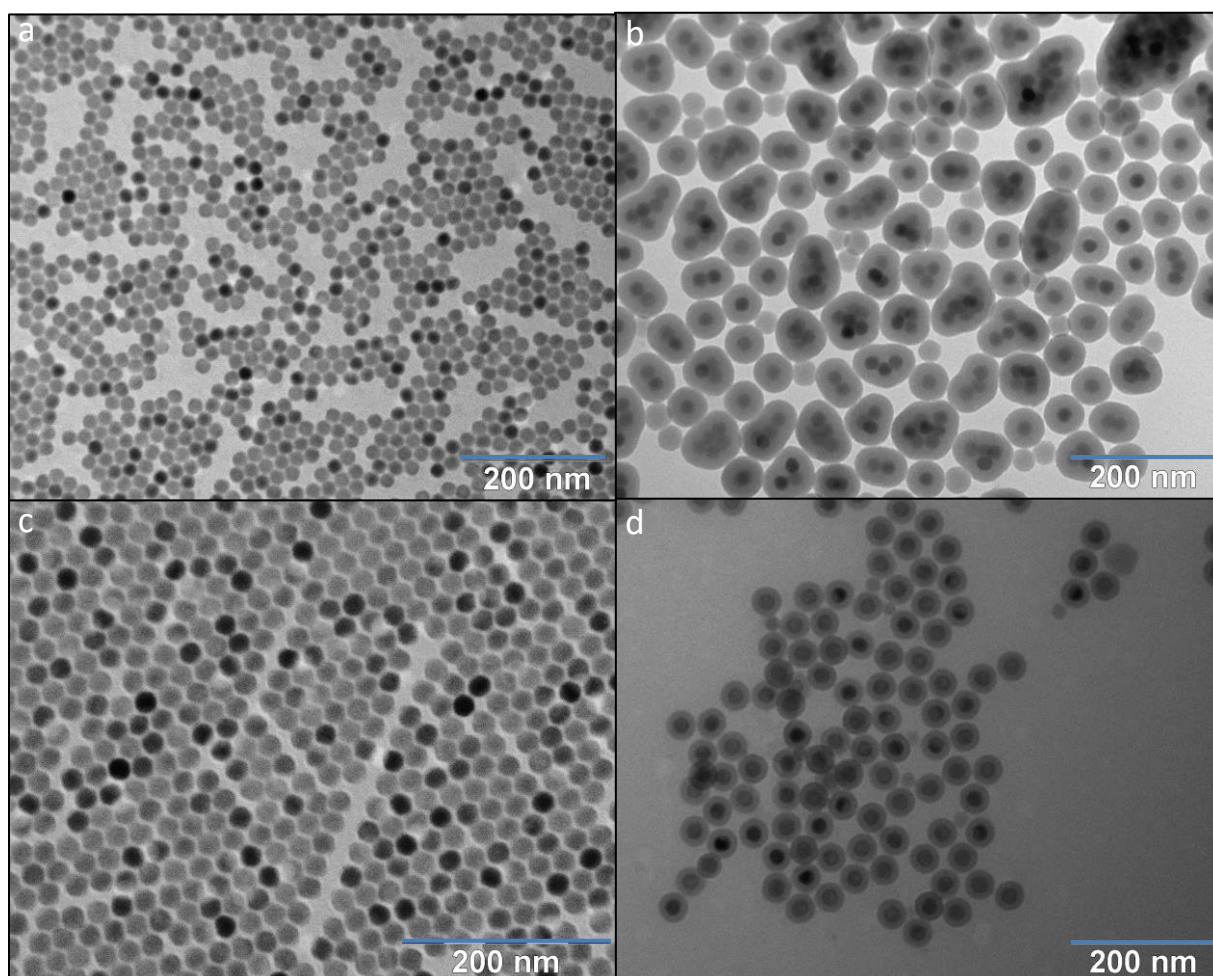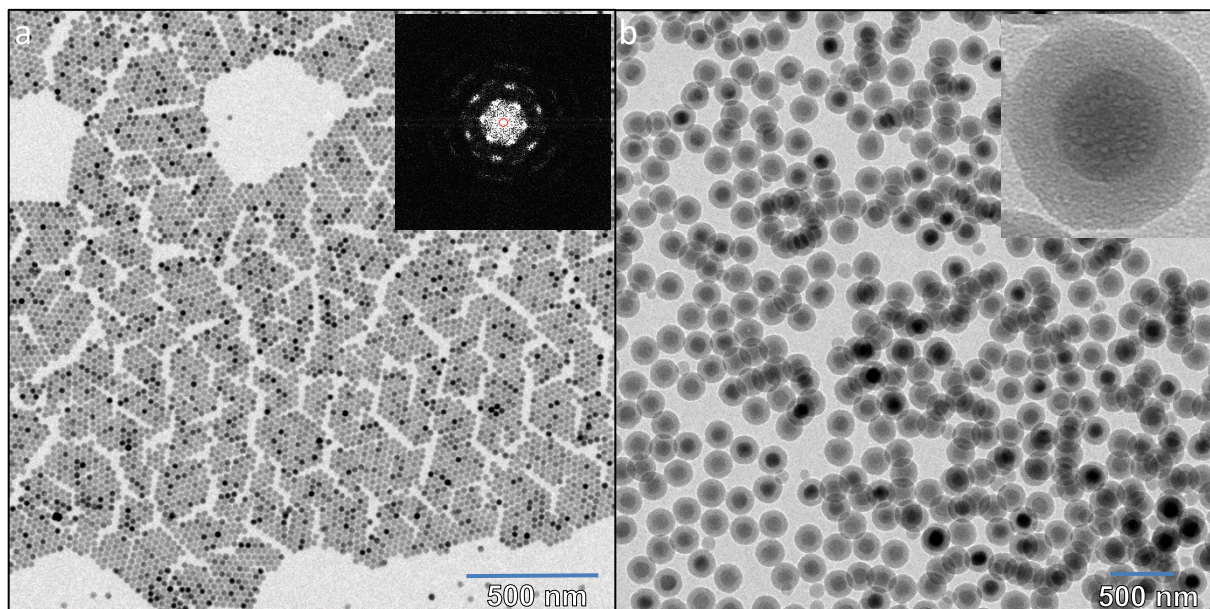

Figure 7 (a) TEM images of the NaYF$_4$ nanocrystals with a low ligand density (b) seem to cluster slightly resulting in multiple nanocrystals in a single silica shell. (c) TEM images of the NaYF$_4$ nanocrystals with a high ligand density (d) subsequently successfully overgrown with a silica shell.

4.2 Structural characterization

By characterizing the nanocrystals shape and size (TEM), elemental composition (EDX), crystallography (XRD) and luminescence properties (luminescence spectroscopy), it is possible to review the nanocrystals and determine if the nanocrystals are successfully synthesized. In this part a comparison is made between the characterization of the $NaYF_4$ nanocrystals and the $NaYF_4@SiO_2$ nanocrystals.

Figure 8 (a) TEM image of the prepared $NaYF_4$ nanocrystals, the inset shows the Fourier Transform representing the long range ordering of the nanocrystals. The average diameter of the monodisperse nanocrystals is *ca*. 22 nm (± 1.1 nm) and the inset shows a well-defined structure. (b) TEM image of the prepared $NaYF_4@SiO_2$ nanocrystals. The inset shows a zoom of one $NaYF_4@SiO_2$ nanocrystals. The shell thickness is *ca.* 10 nm.

A TEM picture of the synthesized nanocrystals is depicted in Figure 8a. The image shows that the synthesis yields monodisperse nanocrystals of 21.7 nm (± 1.1 nm). The nanocrystals are well separated and form hexagonally ordered domains. This is due to the steric effects of the ligand layer and the high monodispersity. The long range ordering of the nanocrystals is illustrated with a Fourier Transform shown in Figure 8a.

In Figure 8b it is shown that the silica growth around the $NaYF_4$ nanocrystals was successful. The silica spheres are >95% filled with individual nanocrystals. The silica shell is grown uniformly around the cores and has a thickness of 10 nm.
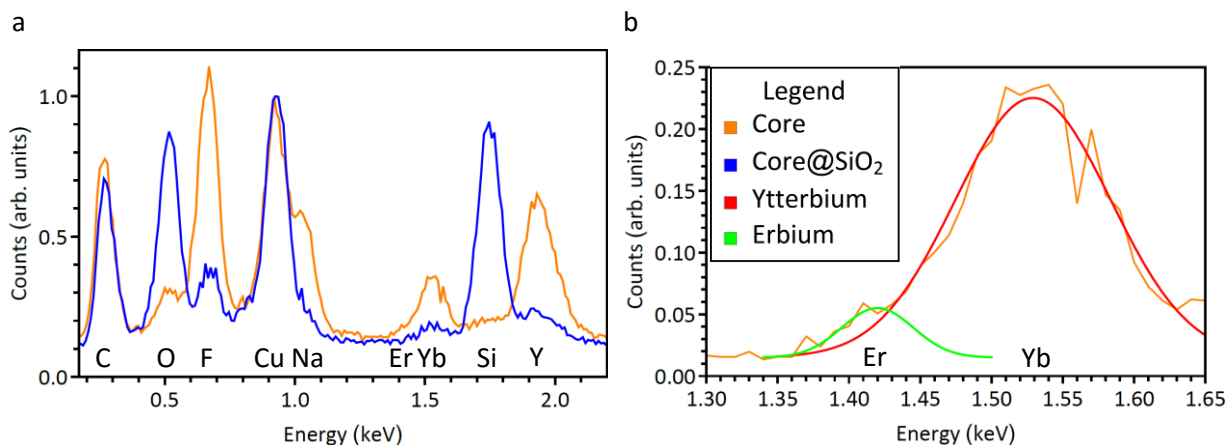
Figure 9 (a) The EDX data shows the presence of Na, YF, Er and Yb, in addition to Cu, C and O. (b) Zoom-in of the Bi-Gaussian signal for Yb and Er. For the NaYF$_4$@SiO$_2$ nanocrystals there is an additional peak due to Si and an increase in the oxygen peak. The two EDX spectra are normalized on the Cu peak.

To investigate the elemental composition of the NaYF$_4$ nanocrystals and the NaYF$_4$@SiO$_2$ nanocrystals, EDX was performed on an area with at least 100 nanocrystals. From the observed peaks in Figure 9a, it can be concluded that Na, Y, F, Er and Yb are all present in the nanocrystals. The C, O and Cu peaks present in the spectrum are due to the carbon film (C, O), the copper TEM grid (Cu), and the ligands around the nanocrystals (C, O). The stoichiometry of all elements (Na:Y:Er:Yb:F) can be calculated by analysing the integrated intensities of the peaks. The rough calculated estimate is 1:0.6:0.02:0.08:3.2 which is in fair agreement with the expected values 1:0.8:0.02:0.18:4. As expected the EDX on the NaYF$_4$@SiO$_2$ nanocrystals shows a similar spectrum, with an additional peak of the element Si. This corresponds with silica overgrowth. The signal in the left EDX from the erbium atoms is already quite weak, zoom in in Figure 9b, and when adding the relatively large amount of silica to the nanocrystals the signal is below the detection limit.
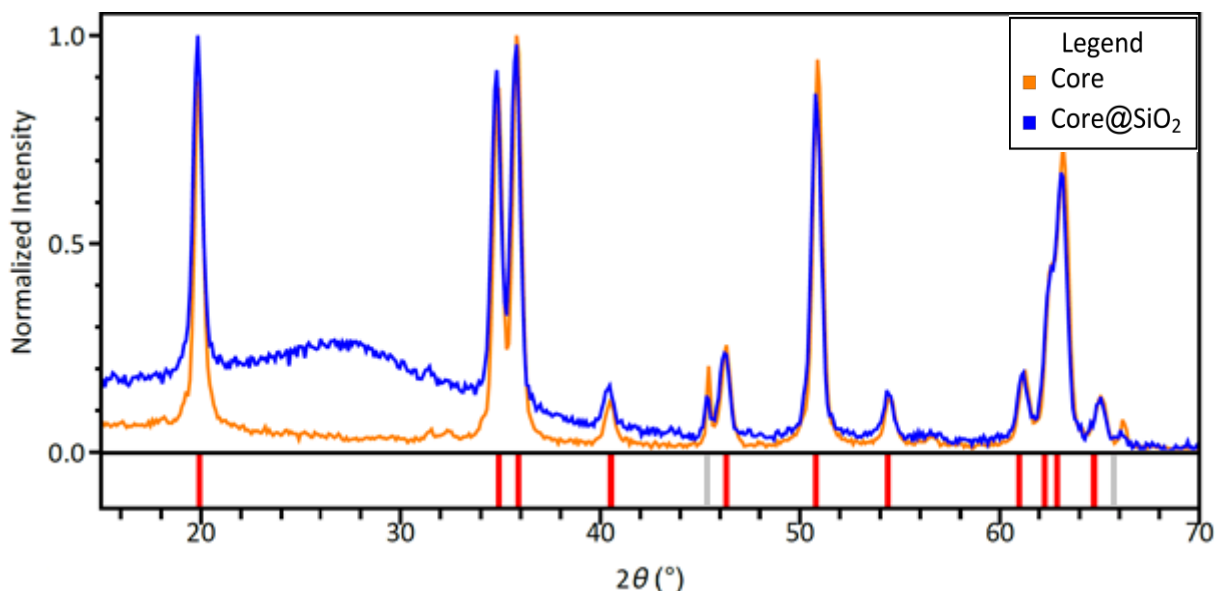
Figure 10 The XRD diffractogram shows the crystallinity of the material. This confirms the hexagonal crystal phase (red, JCPDS No. 00-028-1192 and some NaF contamination (grey, JCPDS No. 00-036-1455). These hexagonal nanocrystals have a crystallite size of *ca.* 18 nm. The NaYF$_4$@SiO$_2$ nanocrystals have an additional broad band due to the amorphous character of silica.

To investigate the crystal phase of the nanocrystals and whether the crystal phase is preserved after silica growth, XRD measurements has been performed. Figure 10 shows that the NaYF$_4$ nanocrystals (orange) and the NaYF$_4$@SiO$_2$ nanocrystals (blue) have the same diffraction peaks, corresponding to the hexagonal phase of NaYF$_4$:Yb^{3+}/Er^{3+} (JCPDS No. 00-028-1192, red lines) and some small NaF

contamination (JCPDS No. 00-036-1455, grey lines). In the diffractogram of the $NaYF_4@SiO_2$ nanocrystals a broad band is present, centred at 27°, which is due to the amorphous silica. The crystallite size can be calculated with the Scherrer equation (Equation 5)[50], where d is the mean crystallite size in nm, λ is the wavelength of the incident X-ray in nm, $\Delta(2\theta)$ is the line broadening at half the maximum intensity (FWHM) in radians, and θ the Bragg angle in degrees.

$$d = \frac{2\sqrt{\frac{\ln 2}{\pi}} \cdot \lambda}{\Delta(2\theta) \cdot \cos\theta} \tag{5}$$

The crystallite size is calculated based on the (201) diffraction peak at a diffraction angle of *ca.* 51°. For the $NaYF_4$ nanocrystals and the $NaYF_4@SiO_2$ nanocrystals this is 19 nm and 18 nm respectively. This rough estimate is in fair accordance with the particle size determined by TEM, which indicates that the particles are monocrystalline and the SiO_2 overgrowth does not affect the $NaYF_4$ cores.

By combining the data from TEM, EDX and XRD it can be concluded that the $NaYF_4$ nanocrystals are monodisperse and monocrystalline with a size of 22 nm. In addition, the silica shell is grown successful around the $NaYF_4@SiO_2$ nanocrystals and the $NaYF_4$ nanocrystals in the core are unaltered.

4.3 Luminescence characterization

To investigate the luminescence properties of the $NaYF_4$ nanocrystals and $NaYF_4@SiO_2$ nanocrystals, (time-resolved) luminescence measurements have been performed as shown in Figure 11 and Figure 12. The measurements were performed using a continuous wave and pulsed laser at 980 nm for the emission and decay measurements respectively.
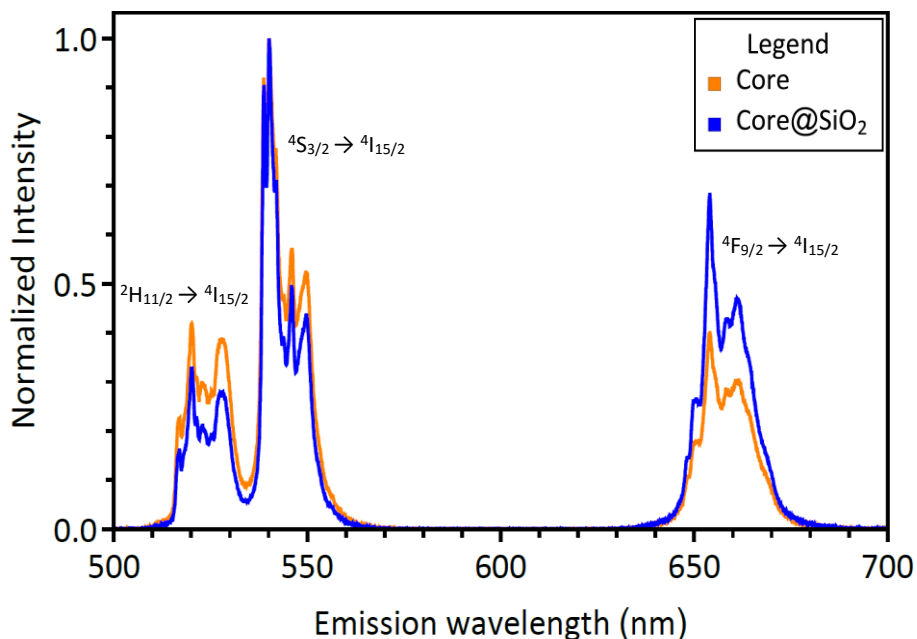
Figure 11 Emission spectrum of the $NaYF_4$ nanocrystals and the $NaYF_4@SiO_2$ nanocrystals between 500 and 700 nm while exciting at 980 nm.

Figure 11 shows the upconversion emission spectra upon excitation of Yb^{3+} in the $^4F_{5/2}$ level at 980 nm. The emission spectra are taken from 500 to 700 nm, showing three distinct peaks, corresponding to the transitions from the $^2H_{11/2}$, $^4S_{3/2}$ and $^4F_{9/2}$ levels to the ground level, $^4I_{15/2}$, as shown in the energy diagram in Figure 4. The levels show splitting by the crystal field, *i.e.* stark-levels.

When we compare the spectra of the NaYF$_4$ nanocrystals and the NaYF$_4$@SiO$_2$ nanocrystals it reveals that the emission spectra are nearly identical. The only notable difference is seen in the relative intensity between the $^2H_{11/2}$ - $^4I_{15/2}$ and $^4F_{9/2}$ - $^4I_{15/2}$ transitions. This can be explained by more relaxation from the $^2H_{11/2}$ excited state to the $^4F_{9/2}$ excited state, probably caused by hydroxyl-vibrations (3000 cm^{-1}) present in silica shell. These vibrations match with the energy gap between the two excited levels. The hydroxyl groups can be present due to incomplete condensation reactions between silanol groups (Si-OH). For complete condensation they form typical silica bonds (Si-O-Si) during the silica overgrowth.
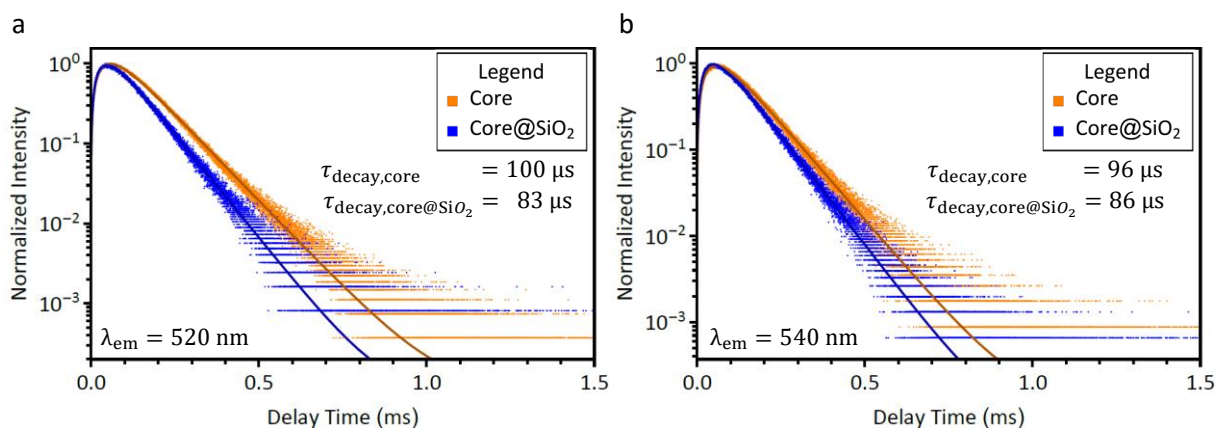
Figure 12 (a) The time-resolved luminescence measurements of the corresponding $^2H_{11/2}$, at 520 nm, and (b) $^4S_{3/2}$, at 540 nm, excited states upon excitation at 980 nm.

In Figure 12a the lifetime of the $^2H_{11/2}$ level and in Figure 12b lifetime of the $^4S_{3/2}$ level are shown. The experimental data is fitted with a bi-exponential fit, shown by the solid lines. The bi-exponent consists of a rise and a decay component. The rise times for both levels are 37 μs and 30 μs for the NaYF$_4$ nanocrystals and the NaYF$_4$@SiO$_2$ nanocrystals respectively. The rise time is due to the upconversion energy transfer from the Yb^{3+} excited states to the Er^{3+} excited states. Because of the energy transfer there is a 'built-up' in the population of the Er^{3+} excited states. The decay times for the NaYF$_4$ nanocrystals are 100 μs and 96 μs for the $^2H_{11/2}$ and $^4S_{3/2}$ levels respectively. The decay times for the NaYF$_4$@SiO$_2$ nanocrystals are 83 μs and 86 μs for the $^2H_{11/2}$ and $^4S_{3/2}$ levels respectively. The lifetime for the NaYF$_4$@SiO$_2$ nanocrystals are expected to be shorter, due to the same effect as observed in the emission spectrum, an increase of nonradiative relaxation, *i.e.* quenching, by hydroxyl-vibrations.

In both the NaYF$_4$ nanocrystals and the NaYF$_4$@SiO$_2$ nanocrystals the decay times are nearly identical for the $^2H_{11/2}$ and $^4S_{3/2}$ levels, proof that they are indeed thermally coupled, *i.e.* the thermal equilibrium establishes much quicker than the radiative and non-radiative rates. As mentioned in the theory the $^2H_{11/2}$ and $^4S_{3/2}$ levels can be thermally coupled because the energy difference between the two levels is within a few K_BT at room temperature. The decay seems fast for forbidden f-f transitions, but this is in accordance with lifetime measurements on bulk material[29]. This can be explained by the small energy gaps between the energy levels in erbium. As explained in the theory, only a few phonons are required to bridge the gap, resulting in fast non-radiative relaxation processes, *i.e.* short lifetimes. However, the QY of the transitions from the $^2H_{11/2}$ and $^4S_{3/2}$ levels is rather low, in the order of 15 %. This is caused by erbium ions on the surfaces and cross-relaxation, as explained in the Chapter 2.

4.4 Temperature dependent luminescent measurements

The $^2H_{11/2}$ and $^4S_{3/2}$ levels show thermally coupled behaviour by the nearly identical measured lifetimes of the two levels. Furthermore, the calculated weighted average energy difference (Equation 6) between the $^2H_{11/2}$ and $^4S_{3/2}$ levels is 711 cm^{-1} and 706 cm^{-1} for the NaYF$_4$ nanocrystals and the NaYF$_4$@SiO$_2$ nanocrystals respectively, corresponding to a few k_BT at room temperature (200 cm^{-1}). To investigate this thermal equilibrium between the two levels and thereby the temperature dependent luminescence, photoluminescence measurements were performed on powders of the NaYF$_4$ nanocrystals and the NaYF$_4$@SiO$_2$ nanocrystals at temperatures from 300 - 600 K and 300 - 900 K respectively, with intervals of 25 K.
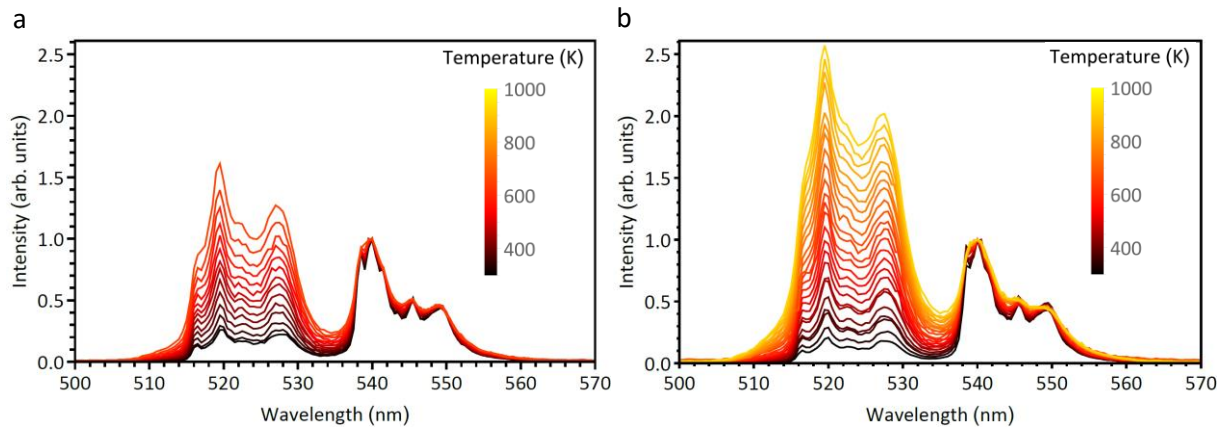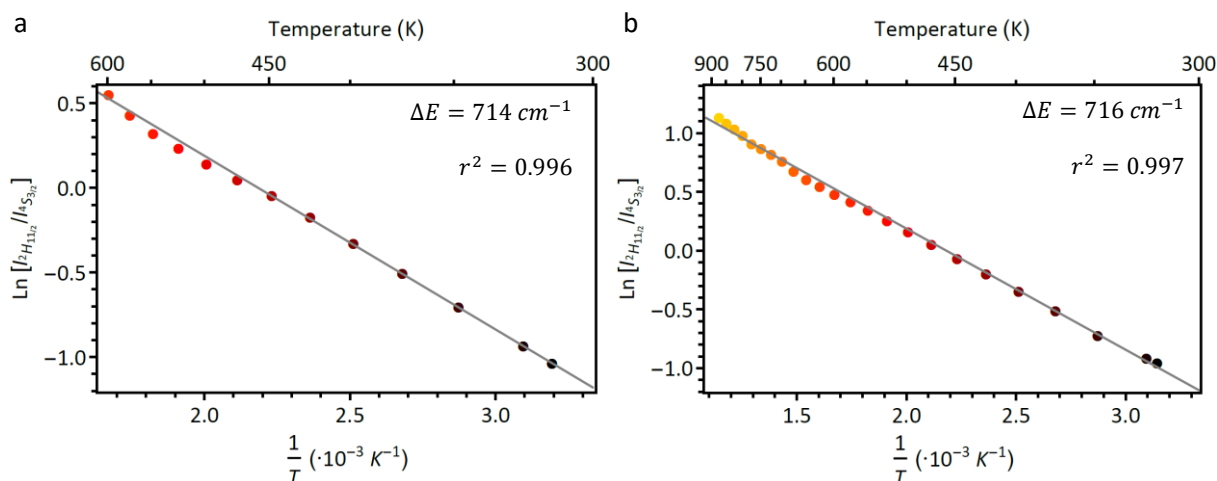

Figure 13 (a) Emission spectra of the NaYF$_4$ nanocrystals and (b) the NaYF$_4$@SiO$_2$ nanocrystals upon excitation at 980 nm taken at temperatures ranging from (a) 300-600 K and (b) 300-900 K with steps of 25 K.

Figure 13 shows spectra upon excitation at 980 nm taken from 300 K (black) up to 600 K (red) and from 300 K up to 900 K (orange) for both the NaYF$_4$ nanocrystals and the NaYF$_4$@SiO$_2$ nanocrystals respectively. The spectra are normalized on the maximum intensity of the $^4S_{3/2} \rightarrow {}^4I_{15/2}$ emission peak. The luminescence decreases with temperature due to the correlation between multiphonon relaxation and temperature. However, when measuring the temperature dependent luminescence of the NaYF$_4$ nanocrystals the luminescence drops below the detection limit above 600 K, where the luminescence of the NaYF$_4$@SiO$_2$ nanocrystals still shows luminescence at 900 K.

Additional to the decreasing luminescence, the relative intensity between the levels changes. The intensity of the higher energy level ($^2H_{11/2}$) increases relatively to the intensity of the lower energy level ($^4S_{3/2}$) by increasing the temperature, indicating that they are thermally coupled. The natural logarithm of this ratio can be plotted versus T^{-1} to obtain a linear dependency as explained in the theory section.

$$\bar{\lambda} = \frac{\sum \lambda_i I_i}{\sum I_i}$$

(6)

Figure 14 The linear relation between the natural logarithm of the integrated intensity ratio of the $^2H_{11/2}$ and $^4S_{3/2}$ emission peaks plotted vs T^{-1} for (a) the $NaYF_4$ nanocrystals and (b) the $NaYF_4@SiO_2$ nanocrystals. Five spectra where measured at every temperature interval to estimate the error in the measurements; this error is within the dot size of the data points.

The natural logarithm of the intensity ratio plotted versus T^{-1} is shown in Figure 14, with a linear model fitted to the experimental data. The coefficient of determination (r^2) of both fits is high; 0.996 and 0.997 for respectively the $NaYF_4$ nanocrystals and the $NaYF_4@SiO_2$ nanocrystals, i.*e.* the linear model represents the data almost perfectly. From the slope of the linear model fit, the energy difference between the excited states, ΔE can be calculated. The value is calculated to be 714 cm^{-1} and 716 cm^{-1} for the $NaYF_4$ nanocrystals and the $NaYF_4@SiO_2$ nanocrystals respectively. This matches closely to the experimental values of ΔE measured from the spectra, respectively 711 cm^{-1} and 706 cm^{-1}.

This relation between temperature and relative luminescence intensities is the main reason to use the nanocrystals as temperature probes. The $NaYF_4$ nanocrystals can be used until 600 K, since the luminescence than suddenly drops and the $NaYF_4@SiO_2$ nanocrystals can be used until 900 K and even higher.

4.5 Temperature dependent structural measurements

To investigate the sudden decrease in luminescence of the core particles, *in situ* XRD has been performed.

The structural changes are investigated upon temperature, by performing *in situ* XRD measurements. The nanocrystals are heated to 550 °C in 9 hours and cooled down rapidly to room temperature in 45 minutes. Simultaneously, XRD measurements of *ca*. 12 minutes were performed to investigate the crystallite size and the crystal phase of the nanocrystals.
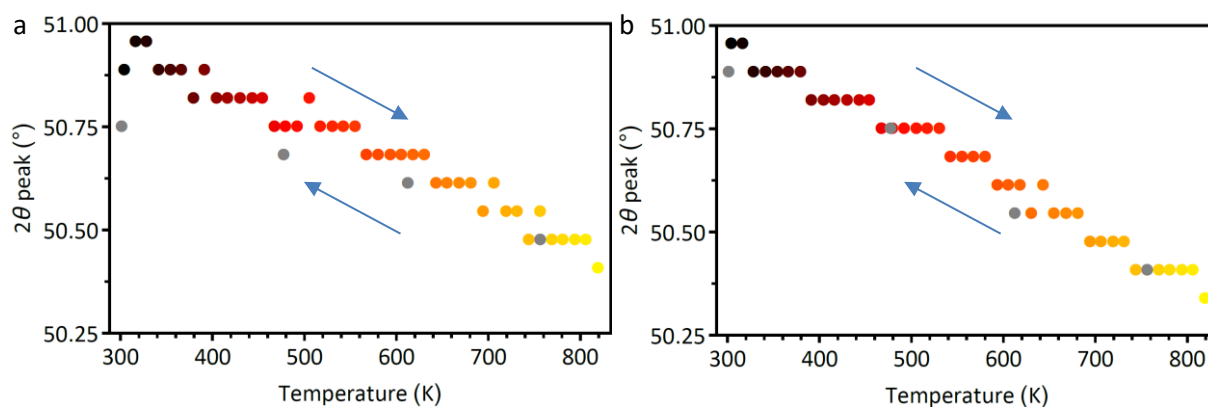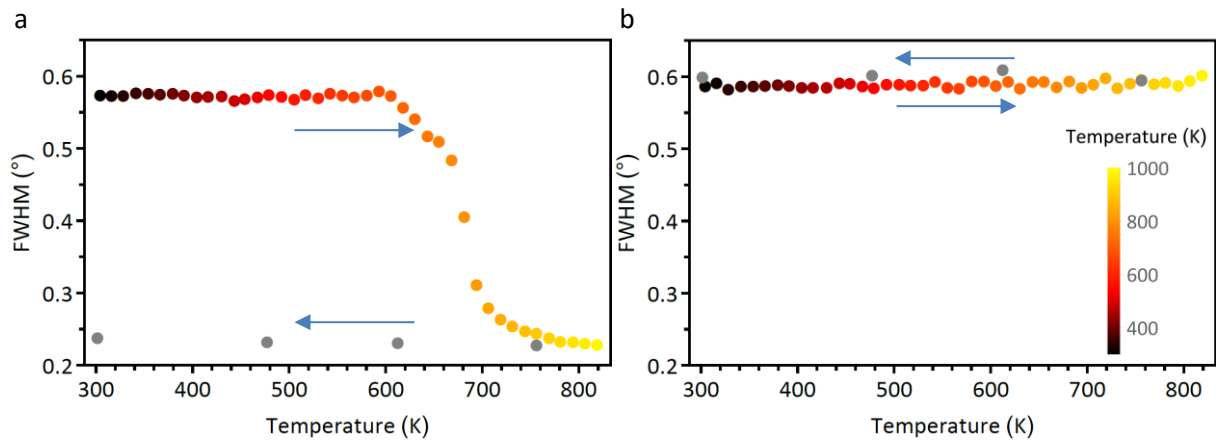

Figure 15 The peak position of (a) the $NaYF_4$ nanocrystals and (b) the $NaYF_4@SiO_2$ nanocrystals of the 201 diffraction peak versus temperature. The grey dots visualize the cooling down.

The XRD diffractograms before, during, and after heating are shown in Appendices E and F for respectively the NaYF$_4$ nanocrystals and the NaYF$_4$@SiO$_2$ nanocrystals. When evaluating the XRD diffractogram no crystal phase transition is observed. Which is in accordance with the phase diagram of the system NaF-YF$_3$ (Figure 20 in Appendices-D)[51–53], where only above 964 K a crystal phase transition from β-phase hexagonal to α-phase cubic crystal phase occurs. The characteristic peaks of hexagonal NaYF$_4$ shift slightly upon heating due to thermal expansion of the crystal lattice, according to

$$a \sim \frac{n\lambda}{2\sin\theta} \tag{7}$$

with a the lattice constant and n an integer. The thermal expansion process is a reversible process as shown in Figure 15 by evaluating the peak position of the 201 crystal surface diffraction peak at increasing and decreasing temperatures.


Figure 16 (a) The FWHM of the NaYF$_4$ nanocrystals and (b) the NaYF$_4$@SiO$_2$ nanocrystals of the 201 diffraction peak versus temperature. The grey dots visualize the cooling down.

However, the diffraction peaks also become irreversible sharper upon heating of the NaYF$_4$ nanocrystals, but not for the NaYF$_4$@SiO$_2$ nanocrystals. To visualize this, the FWHM of the 201 diffraction peak is evaluated as shown in Figure 16 plotted versus the temperature, for (a) the NaYF$_4$ nanocrystals and (b) the NaYF$_4$@SiO$_2$ nanocrystals.

A decrease in FWHM corresponds to an increase in crystallite size according to the Scherrer equation. The decrease for the NaYF$_4$ nanocrystals starts at 600 K and is irreversible upon cooling down. Consequently, the results show that the nanocrystals coalesce and start to grow at 600 K. During the growth of the nanocrystals probably defects are formed, which are quenching sites for the luminescence and therefore explain the sudden decrease in luminescence intensity at the same temperature. This is absent for the NaYF$_4$@SiO$_2$ nanocrystals, which show a constant crystallite size of the NaYF$_4$ nanocrystals, concluding that no coalescence occurs up to 825 K. This corresponds to the luminescence dependent measurements where no luminescence drop occurs up to 900 K. Concluding, the NaYF$_4$@SiO$_2$ can be used for temperature measurements over a wide temperature range.

4.6 Thermal cycling measurements

At this point the $NaYF_4@SiO_2$ nanocrystals have shown temperature dependent upconversion luminescence up to 900 K. However, for being an applicable temperature probe it should be accurate and durable. From Figure 14 the accuracy and temperature range can be obtained, but no information about durability is obtained. To investigate the durability of the nanocrystals, luminescence measurements were performed while cycling five times between room temperature (300 K), 900 K and room temperature (300 K) again. During these cycles, luminescence measurements were performed at 300 K, 425 K, 575 K, 725 K and 900 K.
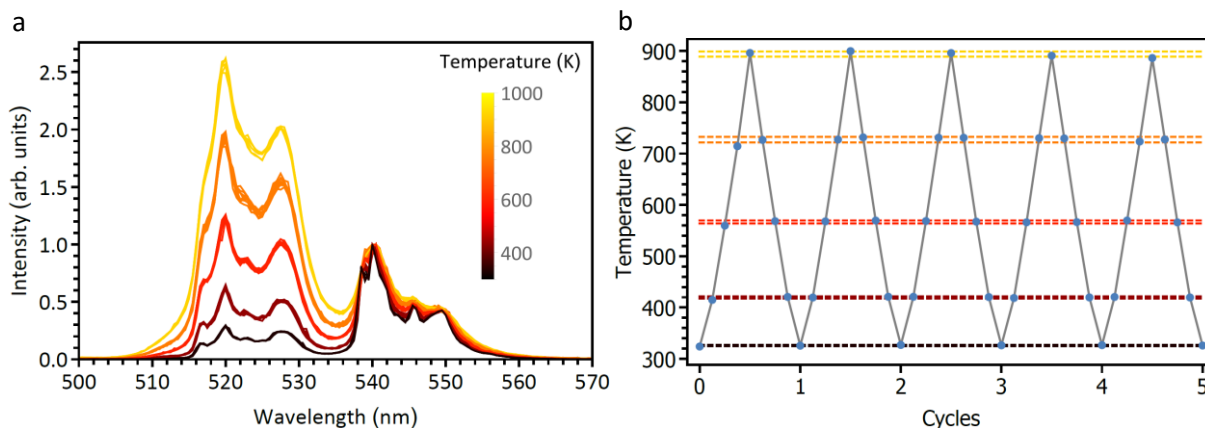
Figure 17 (a) Emission spectra of the $NaYF_4@SiO_2$ nanocrystals upon excitation at 980 nm while cycling the temperature between 300 K and 900 K for 5 times with steps of 150 K. (b) The calculated temperatures from the fluorescent intensity ratio in the emission spectra are plotted per cycle step (blue dots). The dashed lines visualize the mean of the data points with a distribution of plus and minus one deviation.

Figure 17a shows the spectra taken at five different temperatures at five following cycles, normalized on the maximum intensity of the $^4S_{3/2} \rightarrow {}^4I_{15/2}$ emission peak. The temperature is calculated from the fluorescence intensity ratio data for the different temperatures in the cycles, resulting in Figure 17b. All the cycles show identical trends. This is visualized by the dashed lines, representing the mean with a distribution of plus and minus one standard deviation of the data points at a certain temperature. These deviations in the temperature are 1.1 K, 1.8 K, 2.9 K, 5.2 K and 5.3 K for 300 K, 450 K, 600 K, 750 K and 900 K respectively.

5 Conclusion

In this work the temperature dependent upconversion luminescence of $NaYF_4$:Yb^{3+}/Er^{3+} nanocrystals is characterized over a large temperature range, relevant for thermometry in chemical reactors. The temperature of the nanocrystals determines the intensity ratio between the two green emission lines of erbium from the $^2H_{11/2}$ level centred at 520 nm and from the $^4S_{3/2}$ level centred at 540 nm. To this end, the green luminescence of erbium is monitored for different temperatures. The green emission of erbium is visible upon infrared excitation of ytterbium at 980 nm and following energy transfer upconversion. To allow for practical application of $NaYF_4$: Yb^{3+}/Er^{3+} as nanothermometer, the scale of nanocrystal synthesis is increased by a factor of four compared to existing procedures. The resulting monodisperse $NaYF_4$ nanocrystals have a size of 22 nm (± 1 nm) and show temperature dependent upconversion luminescence up to 600 K. Above this temperature the $NaYF_4$ nanocrystals melt together and the luminescence drops. A silica shell of *ca.* 10 nm has been grown around the $NaYF_4$ nanocrystals to overcome this problem. The resulting $NaYF_4$@SiO_2 nanocrystals show temperature dependent luminescence up to 900 K. The intensity ratio between the $^2H_{11/2}$ level and the $^4S_{3/2}$ level changes from *ca.* 0.4 at 300 K to *ca.* 3 at 900 K. The temperature variations of the intensity ratio are identical for five consecutive cycles, showing that the durability of the $NaYF_4$@SiO_2 nanocrystals is high. The accuracy of the measurements is high, with standard deviations of 1 K and 5 K below and above 750 K.

Our results show that $NaYF_4$:Yb^{3+}/Er^{3+} nanocrystals can be used as a non-invasive thermometer up to 900 K after encapsulation in a protective silica shell. The broad temperature range, temperature resolution, and durability make that this system can be used to measure temperature variations inside a chemical reactor.

6 Outlook

In this chapter future experiments will be discussed.

6.1 Synthesis

- For the synthesis of the β-NaYF$_4$ nanocrystals, lanthanide acetate hydrates are used as reactants. The amount of water in these hydrates is not well defined and gives uncertainty in number of reactants. It would be useful to determine the amount of water in the lanthanide acetates hydrates, or even better to use dehydrated lanthanide acetates only.
- In chapter 3 (page 16) the formation of hexagonal β-NaYF$_4$ nanocrystals is discussed. The nucleation of the β-particles is initiated by dissolving the cubic α-NaYF$_4$ nanocrystals at elevated temperatures, *i.e.* the α-particles are a precursor for the β-particles. This gives rise to a different method of synthesizing NaYF$_4$ nanocrystals, yielding new possibilities[48,54], *i.e.* an even higher yield than in this work, more monodisperse nanocrystals, reproducible way of synthesizing different sizes of nanocrystals, and also possibilities to make multi-shell structure with interesting luminescence properties. Especially the first is interesting for the scope of this research.
- Growth of an inactive NaYF$_4$ shell around the nanocrystal to decrease surface quenching (Figure 18), resulting in higher luminescent nanocrystals as discussed in 2.3.1 Energy transfer to defects[55].
- Impregnation of the nanocrystals in a catalytic host material, *i.e.* extrudate with mesopores of 2 - 50 nm size.
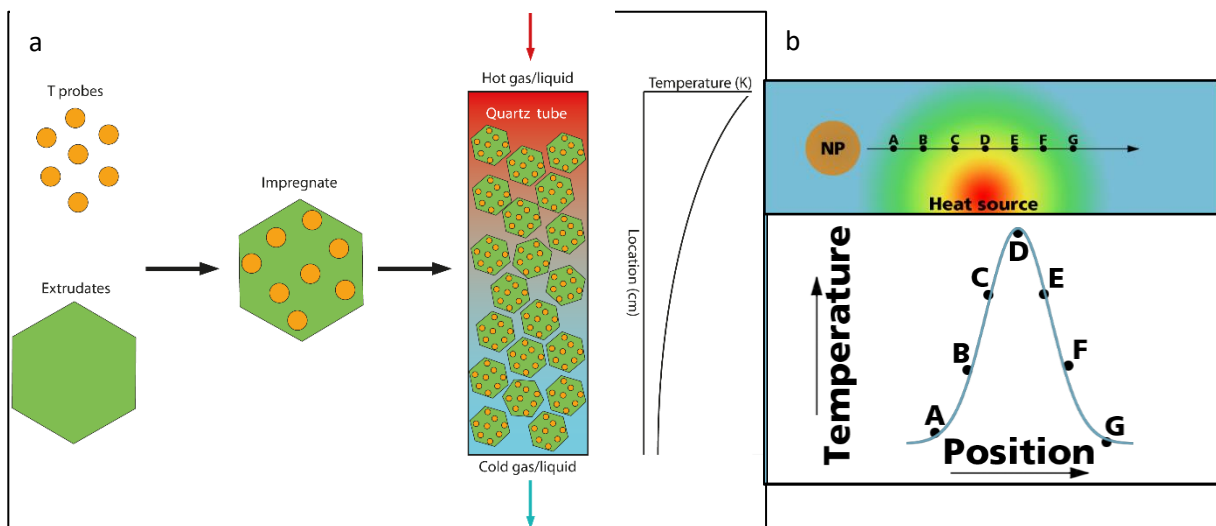
6.2 Measurements

- More temperature cycles for further investigation of the durability of the nanocrystals.
- CCD to improve temporal resolution, because in this work the luminescence measurements took 14 seconds at the different temperatures.
- Use a confocal microscope to improve spatial resolution[6,7,56], because in this work there is no research done on the spatial resolution.
- Temperature measurements in more chemical reactor-like set-up (Figure 19a).
  - Nanocrystals impregnated in extrudates
  - Glass or quarts reactor tube
- Luminescence and structural measurements to a higher temperature, to determine the maximum temperature for the silica coated nanocrystals. Interesting is what happens around 960 K, where according to the phase-diagram (Figure 20)[51–53], a phase transition occurs.
- Test chemical stability of the uncoated and coated nanocrystals in environments relevant for chemical reactors.

6.3 Additional research

- Optical tweezers and single particle spectroscopy[57] can be used to guide nanocrystals past a well-defined heat source (Figure 19b).
  - This can give information about the spatial and temporal temperature response of the nanocrystals.
- Other host materials and lanthanide couples
  - Great variety in different host materials for lanthanide ions, especially other fluorides and oxides are interesting because of low phonon vibrations in the lattice. Additional other lanthanide couples are interesting for example Pr^{3+}, excited and emitting in the IR, where there is high penetration.
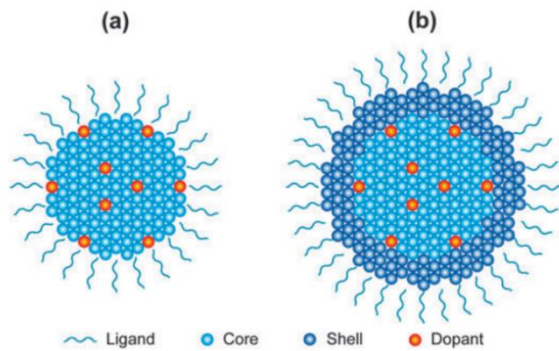
Figure 18 Proposed statistical distributions of lanthanide dopants in (a) a nanocrystal without the protection of a shell and (b) a core-shell type nanocrystal. The non-protected nanocrystal features a relatively large number of surface dopant ions that are poorly luminescent. In contrast, all dopant ions in the core-shell nanocrystal are confined in the interior core of the crystal and participate in efficient luminescence[55].

Figure 19 (a) A schematic view of impregnation of the nanocrystals in extrudates and possible measurement set-up. (b) A schematic view of a nanoparticle guided past a well-defined heat source. Schematics by Robin Geitenbeek.

7 Acknowledgements

This work would not have been accomplished with the help of many people and therefore I would like to thank them here.

First of all, I would like to thank Robin Geitenbeek for the daily supervision and support during my master thesis. I started this master program without a lot of experience in chemistry and you helped me to develop all my current knowledge in both synthesis and spectroscopy. You have put a lot of time in the supervision, which made my master thesis a success for me. I really appreciate involving me in most of your PhD project.

Secondly, I would like to thank Andries Meijerink for supervision during this project. "Your door was always open" to discuss the results, which really motivated me along the way. I felt especially encouraged when you showed up during spectroscopic measurements, because you were interested in our work.

Thirdly, I would like to thank some other people. Freddy Rabouw for helping me with the analysis of data (Mathematica) and for the help with spectroscopic measurements. My fellow master student Marieke Castelijns for all the discussions about upconversion, which resulted in a jointed project, initiated by ourselves and encouraged by our supervisors. The project was even such a success that we are writing a paper about the results.

Finally, I would like to thank all students, PhD's, and staff members of the CMI group. I had a great time the past one and a half year I was there. All of you contributed to the scientific interest and fun time I had with you. I really enjoyed the social group activities with you all!

References

1. Brites, C. D. S. *et al.* Thermometry at the nanoscale. *Nanoscale* **4,** 4799–4829 (2012).

2. Jaque, D. & Vetrone, F. Luminescence nanothermometry. *Nanoscale* **4,** 4301–4326 (2012).

3. Lee, J. & Kotov, N. Thermometer design at the nanoscale. *Nano Today* **2,** 48–51 (2007).

4. McLaurin, E. J., Vlaskin, V. A. & Gamelin, D. R. Water-Soluble Dual-Emitting Nanocrystals for Ratiometric Optical Thermometry. *J. Am. Chem. Soc.* **133,** 14978–14980 (2011).

5. Chandrasekharan, N. & Kelly, L. A. A Dual Fluorescence Temperature Sensor Based on Perylene/Exciplex Interconversion. *J. Am. Chem. Soc.* **123,** 9898–9899 (2001).

6. Vetrone, F. *et al.* Intracellular imaging of HeLa cells by non-functionalized NaYF4 : Er3+, Yb3+ upconverting nanoparticles. *Nanoscale* **2,** 495–8 (2010).

7. Vetrone, F. *et al.* Temperature Sensing Using Fluorescent Nanothermometers. *ACS Nano* **4,** 3254–3258 (2010).

8. Suzuki, M., Tseeb, V., Oyama, K. & Ishiwata, S. Microscopic Detection of Thermogenesis in a Single HeLa Cell. *Biophys. J.* **92,** L46–L48 (2007).

9. Zhao, Y. *et al.* High-Temperature Luminescence Quenching of Colloidal Quantum Dots. *ACS Nano* **6,** 9058–9067 (2012).

10. Klaine, S. J. *et al.* Nanomaterials in the environment: Behavior, fate, bioavailability, and effects. *Environ. Toxicol. Chem.* **27,** 1825 (2008).

11. Blasse, G. B. & Grabmaier, B. C. *Luminescent Materials*. (Springer Berlin Heidelberg, 1994).

12. Wade, S. a., Collins, S. F. & Baxter, G. W. Fluorescence intensity ratio technique for optical fiber point temperature sensing. *J. Appl. Phys.* **94,** 4743 (2003).

13. Kusama, H., Sovers, O. & Yoshioka, T. Line shift method for phosphor temperature measurements. *Jpn. J. Appl. Phys.* **15,** 2349–2358 (1976).

14. Fischer, L. H., Harms, G. S. & Wolfbeis, O. S. Upconverting nanoparticles for nanoscale thermometry. *Angew. Chem. Int. Ed. Engl.* **50,** 4546–51 (2011).

15. Wang, F. & Liu, X. Recent advances in the chemistry of lanthanide-doped upconversion nanocrystals. *Chem. Soc. Rev.* **38,** 976–89 (2009).

16. Wang, F., Banerjee, D., Liu, Y., Chen, X. & Liu, X. Upconversion nanoparticles in biological labeling, imaging, and therapy. *Analyst* **135,** 1839 (2010).

17. Auzel, F. Upconversion and Anti-Stokes Processes with f and d Ions in Solids. *Chem. Rev.* **104,** 139–173 (2004).

18. Chorkendorff, I. & Niemantsverdriet, J. W. *Concepts of Modern Catalysis and Kinetics*. (2003).

19. Hartmann, J., Voigt, P. & Reichling, M. Measuring local thermal conductivity in polycrystalline diamond with a high resolution photothermal microscope. *J. Appl. Phys.* **81,** 2966 (1997).

20. Maldague, X. & Marinetti, S. Pulse phase infrared thermography. *NDT E Int.* **29,** 391 (1996).

21. Singh, S. K., Kumar, K. & Rai, S. B. Er3+/Yb3+ codoped Gd2O3 nano-phosphor for optical thermometry. *Sensors Actuators A Phys.* **149,** 16–20 (2009).

22. Ball, D. *Physical Chemistry*. (2002).

23. Freeman, A. J. & Watson, R. E. Theoretical Investigation of Some Magnetic and Spectroscopic Properties of Rare-Earth Ions. *Phys. Rev.* **127,** 2058–2075 (1962).

24. Kenyon, A. J. Recent developments in rare-earth doped materials for optoelectronics. *Prog. Quantum Electron.* **26,** 225–284 (2002).

25. Dieke, Gerhard, H. *Spectra and energy levels of rare earth ions in crystals. American Journal of Physics* **38,** (Interscience Publishers, 1968).

26. Wegh, R., Meijerink, A., Lamminmäki, R. & Hölsä, J. Extending Dieke's diagram. *J. Lumin.* **89,** 1002–1004 (2000).

27. Krämer, K. W. *et al.* Hexagonal Sodium Yttrium Fluoride Based Green and Blue Emitting Upconversion Phosphors. *Chem. Mater.* **16,** 1244–1251 (2004).

28. Egorov, S. A. & Skinner, J. L. On the theory of multiphonon relaxation rates in solids. *J. Chem. Phys.* **103,** 1533–1543 (1995).

29. Suyver, J. F. *et al.* Upconversion spectroscopy and properties of NaYF4 doped with Er3+, Tm3+ and/or Yb3+. *J. Lumin.* **117,** 1–12 (2006).

30. Förster, T. Zwischenmolekulare Energiewanderung und Fluoreszenz. *Ann. Phys.* **437,** 55–75 (1948).

31. Wang, F. & Liu, X. Upconversion multicolor fine-tuning: visible to near-infrared emission from lanthanide-doped NaYF4 nanoparticles. *J. Am. Chem. Soc.* 5642–5643 (2008).

32. Boyer, J.-C. & van Veggel, F. C. J. M. Absolute quantum yield measurements of colloidal NaYF4: Er3+, Yb3+ upconverting nanoparticles. *Nanoscale* **2,** 1417–9 (2010).

33. Heer, S., Kömpe, K., Güdel, H. U. & Haase, M. Highly efficient multicolour upconversion emission in transparent colloids of lanthanide-doped NaYF4 nanocrystals. *Adv. Mater.* **16,** 2102–2105 (2004).

34. Renero-Lecuna, C. *et al.* Origin of the High Upconversion Green Luminescence Efficiency in β-NaYF 4 :2%Er 3+ ,20%Yb 3+. *Chem. Mater.* **23,** 3442–3448 (2011).

35. Suyver, J. F., Grimm, J., Krämer, K. W. & Güdel, H. U. Highly efficient near-infrared to visible up-conversion process in NaYF4:Er3+,Yb3+. *J. Lumin.* **114,** 53–59 (2005).

36. Strohhöfer, C. & Polman, A. Absorption and emission spectroscopy in Er3+–Yb3+ doped aluminum oxide waveguides. *Opt. Mater. (Amst).* **21,** 705–712 (2003).

37. Atkins, P. & Paula, J. de. *Atkins' Physical Chemistry*. (OUP Oxford, 2014).

38. Lakowicz, J. R. *Principles of Fluorescence Spectroscopy*. (Springer US, 2006).

39. Svelto, O. *Principles of Lasers*. (Springer US, 2010).

40. Planck, M. Ueber das Gesetz der Energieverteilung im Normalspectrum. *Ann. Phys.* **309,** 553–563 (1901).

41. Collins, S. F. *et al.* Comparison of fluorescence-based temperature sensor schemes: Theoretical analysis and experimental validation. *Journal of Applied Physics* **84,** 4649–4654 (1998).

42. McLaurin, E. J., Bradshaw, L. R. & Gamelin, D. R. Dual-emitting nanoscale temperature sensors. *Chem. Mater.* **25,** 1283–1292 (2013).

43. Mai, H.-X., Zhang, Y.-W., Sun, L.-D. & Yan, C.-H. Size- and Phase-Controlled Synthesis of Monodisperse NaYF 4 :Yb,Er Nanocrystals from a Unique Delayed Nucleation Pathway Monitored with Upconversion Spectroscopy. *J. Phys. Chem. C* **111,** 13730–13739 (2007).

44. Wang, X., Zhuang, J., Peng, Q. & Li, Y. A general strategy for nanocrystal synthesis. *Nature* **437,** 121–4 (2005).

45. Li, Z. & Zhang, Y. An efficient and user-friendly method for the synthesis of hexagonal-phase NaYF 4 :Yb, Er/Tm nanocrystals with controllable shape and upconversion fluorescence. *Nanotechnology* **19,** 345606 (2008).

46. Wang, F., Deng, R. & Liu, X. Preparation of core-shell NaGdF4 nanoparticles doped with luminescent lanthanide ions to be used as upconversion-based probes. *Nat. Protoc.* **9,** 1634–1644 (2014).

47. Rinkel, T., Nordmann, J., Raj, A. N. & Haase, M. Ostwald-ripening and particle size focussing of sub-10 nm NaYF 4 upconversion nanocrystals. *Nanoscale* **6,** 14523–14530 (2014).

48. Nordmann, J. *et al.* Synthesis of β-Phase NaYF4:Yb,Er Upconversion Nanocrystals and Nanorods by Hot-Injection of Small Particles of the α-Phase. *Zeitschrift für Phys. Chemie* **229,** 247–262 (2015).

49. Koole, R. *et al.* On the Incorporation Mechanism of Hydrophobic Quantum Dots in Silica Spheres by a Reverse Microemulsion Method. *Chem. Mater.* **20,** 2503–2512 (2008).

50. Scherrer, P. Bestimmung der Größe und der inneren Struktur von Kolloidteilchen mittels Röntgenstrahlen. *Nachrichten von der Gesellschaft der Wissenschaften zu Göttingen, Math. Klasse* 98–100 (1918).

51. Thoma, R. E., Hebert, G. M., Insley, H. & Weaver, C. F. Phase Equilibria in the System Sodium Fluoride-Yttrium Fluoride. *Inorg. Chem.* **2,** 1005–1012 (1963).

52. Fedorov, P. P. *et al.* Phase diagrams of the NaF-RF₃ (R = Tb, Dy, Er) systems. *Zhurnal Neorg. Khimii* **41,** 1715–1719 (1996).

53. Sobolev, B. P. *The Rare Earth Trifluorides: The high temperature chemistry of the rare earth trifluorides*. (2000).

54. Johnson, N. J. J., Korinek, A., Dong, C. & van Veggel, F. C. J. M. Self-Focusing by Ostwald Ripening: A Strategy for Layer-by-Layer Epitaxial Growth on Upconverting Nanocrystals. *J. Am. Chem. Soc.* **134,** 11068–11071 (2012).

55. Wang, F., Wang, J. & Liu, X. Direct Evidence of a Surface Quenching Effect on Size-Dependent Luminescence of Upconversion Nanoparticles. *Angew. Chemie* **49,** 7456–7460 (2010).

56. Gargas, D. J. *et al.* Engineering bright sub-10-nm upconverting nanocrystals for single-molecule imaging. *Nat. Nanotechnol.* **9,** 300–305 (2014).

57. Rodríguez-Sevilla, P. *et al.* Assessing Single Upconverting Nanoparticle Luminescence by Optical Tweezers. *Nano Lett.* **15,** 5068–5074 (2015).

Appendices
A Synthesis of NaYF$_4$:Yb/Er (80/18/2)

- Add 4 mmol rare-earth acetate (851.32 mg yttrium, 252.12 mg ytterbium and 27.55 mg erbium) and 24 mL of OA and 68 mL of ODE to a 250 mL three-neck round-bottom flask (note: max volume will be 132 ml).
- Degas the mixture on a vacuum Schlenk-line at RT and afterwards for 90 min at 120 °C under vigorous stirring (*ca.* 1200 rpm).
- After flushing the Schlenk-line by cycle three times between nitrogen and vacuum, cool down to room temperature with a gentle flow of nitrogen gas, through the reaction flask while stirring.
- Under nitrogen slowly add first 10 mmol of NaOH (399.97 mg) and second 16 mmol of NH$_4$F (592.64 mg) dissolved in respectively 10 and 30 ml, to the flask and stir vigorously (*ca.* 1200 rpm) overnight.
- Increase the temperature to 100 °C. Next, keep the reaction mixture under vacuum for 30 minutes.
- On the next day, remove the methanol at *ca.* 65 °C.
- Increase the temperature to 100 °C. Next, keep the reaction mixture under vacuum for 30 minutes. Flush the Schlenk-line by cycle three times between nitrogen and vacuum.
- Under a nitrogen flow and vigorous stirring (*ca.* 1200 rpm), heat the mixture to 300 °C (with a heating rate of *ca.* 10 °C/min) and keep at this temperature for 110 minutes.
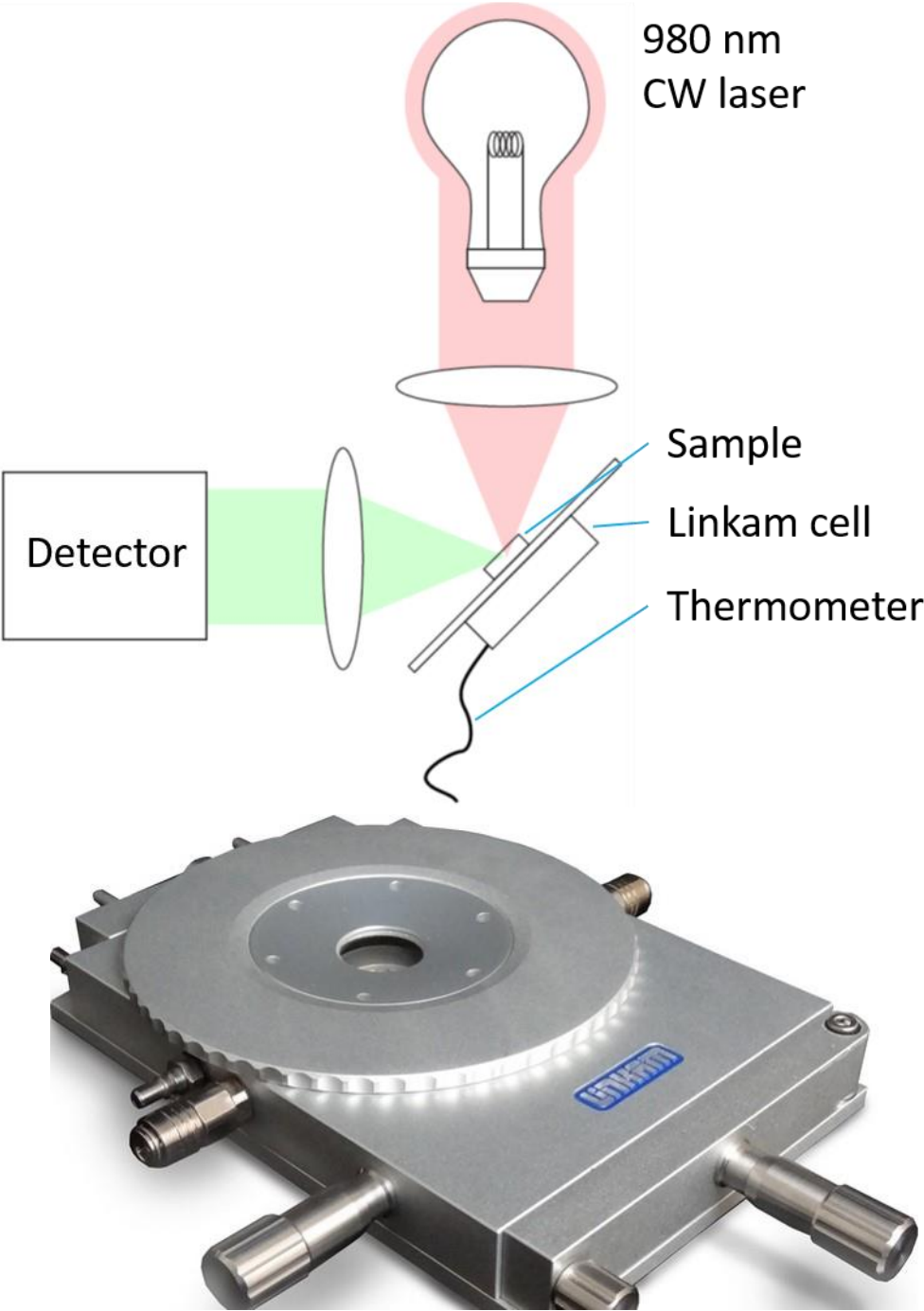- Cool down to room temperature while stirring.

Precipitation

- Merge the clear supernatant with an equal volume of ethanol (80 ml) leading to precipitation of the nanocrystals and separated by centrifugation for 8 min at 2500 rpm.
- Purify the particles by redispersing the precipitate in 12 mL cyclohexane and precipitate with ethanol and separate by centrifugation repeat this two times.
- Re-disperse the precipitate in 12 mL cyclohexane than add 12 mL OA and mix, precipitate with ethanol and separate by centrifugation.
- Re-disperse in 12 mL cyclohexane.
- Dilute 1:20 for TEM sample.

B Synthesis of Silica shell

- Disperse 13 g of NP-5 in 108 mL of cyclohexane in a 250 mL one-neck round-bottom flask.
- Stir the reaction mixture for 15 minutes (850 rpm).
- Add **2.125 mL (100 mg) NaYF$_4$ particles (5 nmol)** dispersed in cyclohexane (before adding, 30 minutes in ultrasonic bath).
- Stir the reaction mixture for 15 minutes (850 rpm).
- Add 800 µL of TEOS.
- Stir the reaction mixture for 15 minutes (850 rpm).
- Add 1500 µL of ammonia.
- After the last step, stir the mixture for 1 min and store it in the dark at room temperature for **24 hours (11.00-11.00)**.
- Destroy the micelles by adding 30 mL of ethanol to the reaction mixture and centrifuging this for 10 min at 2000g and remove the supernatant.
- Purify the NaYF$_4$@SiO$_2$ nanocrystals by adding 100 mL of ethanol and centrifuging this for 20 min at 2000g and remove the ethanol.
- Purify the NaYF$_4$@SiO$_2$ nanocrystals by adding 100 mL of ethanol and centrifuging this for 40 min at 2000g and remove the ethanol.
- Disperse the purified NaYF$_4$@SiO$_2$ nanocrystals in 10 mL ethanol.
- For a TEM sample dilute 1:10.

C Temperature dependent luminescence measurements set-up

980 nm
CW laser

Sample

Detector

Linkam cell

Thermometer

D Phase diagram NaYF₄

A   LIQUID
B   NaF + LIQUID
C   NaF + HEXAGONAL NaF·YF₃
D   HEXAGONAL NaF·YF₃ + LIQUID
E   FLUORITE CUBIC NaF·YF₃ – 5NaF·9YF₃ SOLID SOLUTION + LIQUID
F   FLUORITE CUBIC NaF·YF₃ – 5NaF·9YF₃ SOLID SOLUTION
G   HEXAGONAL NaF·YF₃ ss + CUBIC NaF·YF₃ – 5NaF·9YF₃ ss
H   CUBIC NaF·YF₃ – 5NaF·9YF₃ ss + ORDERED 5NaF·9YF₃ ss

I   HEXAGONAL NaF·YF₃ ss
J   HEXAGONAL NaF·YF₃ ss + ORDERED 5NaF·9YF₃ ss
K   ORDERED 5NaF·9YF₃ ss
L   HEXAGONAL NaF·YF₃ ss + ORTHORHOMBIC YF₃
M   ORDERED 5NaF·9YF₃ + ORTHORHOMBIC YF₃
N   CUBIC 5NaF·9YF₃ + ORTHORHOMBIC YF₃
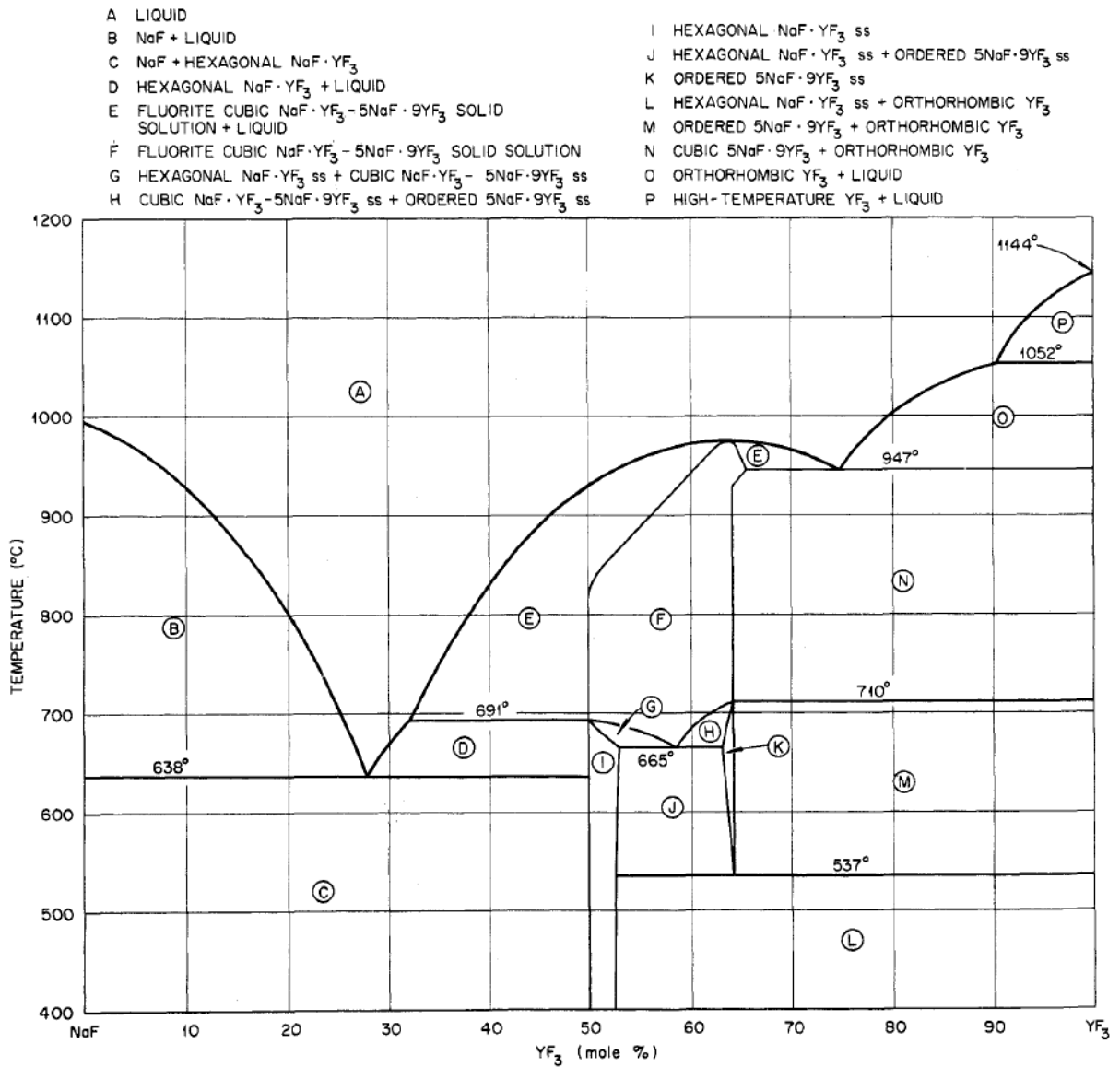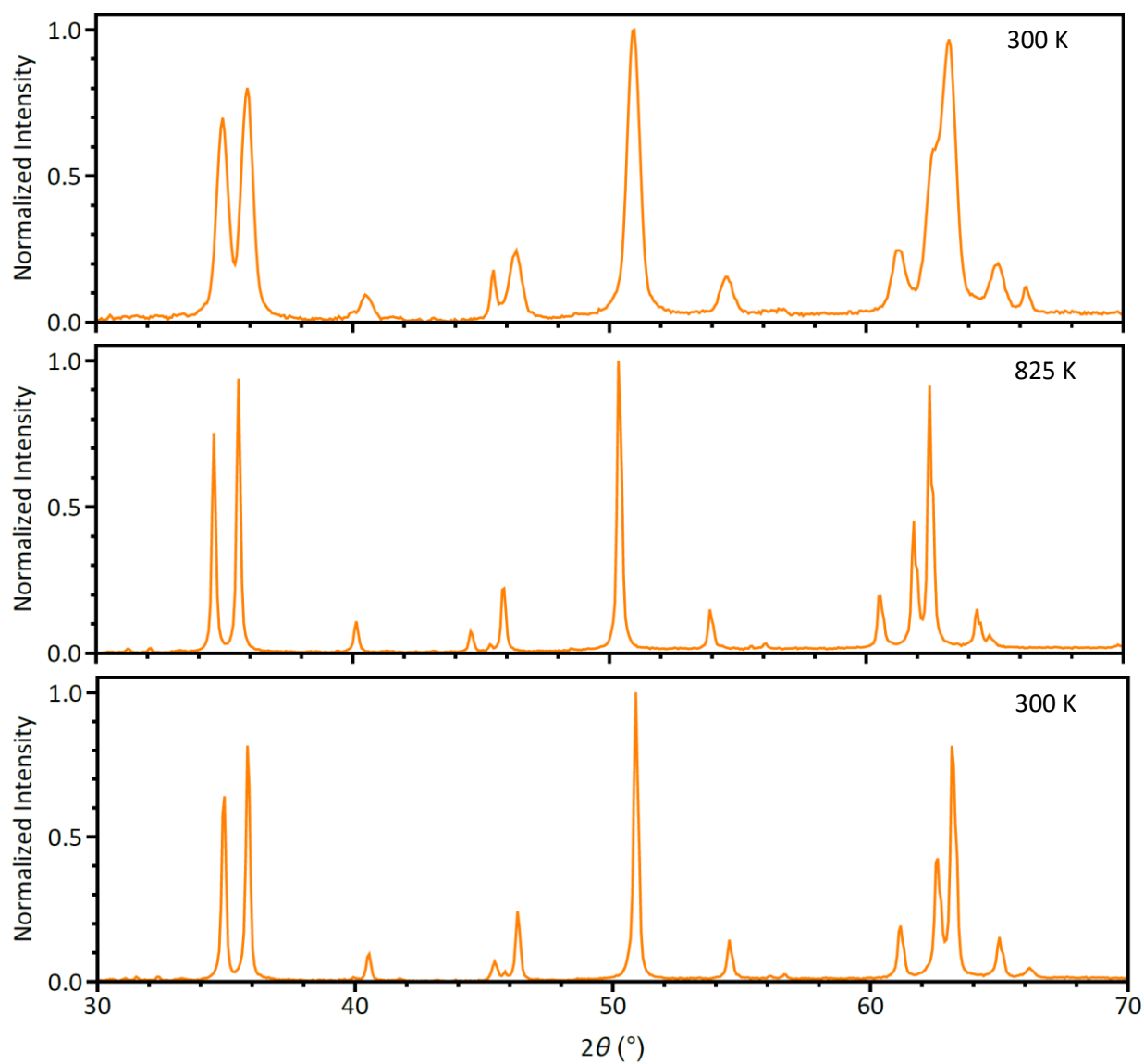O   ORTHORHOMBIC YF₃ + LIQUID
P   HIGH-TEMPERATURE YF₃ + LIQUID

Figure 20 Phase diagram of the system NaF-YF₃[51]. A phase transition occurs from hexagonal NaYF₄ (I) to cubic NaYF₄ (E and F) at 964 K. This diagram is in accordance with Fedorov[52] and Sobolev[53].
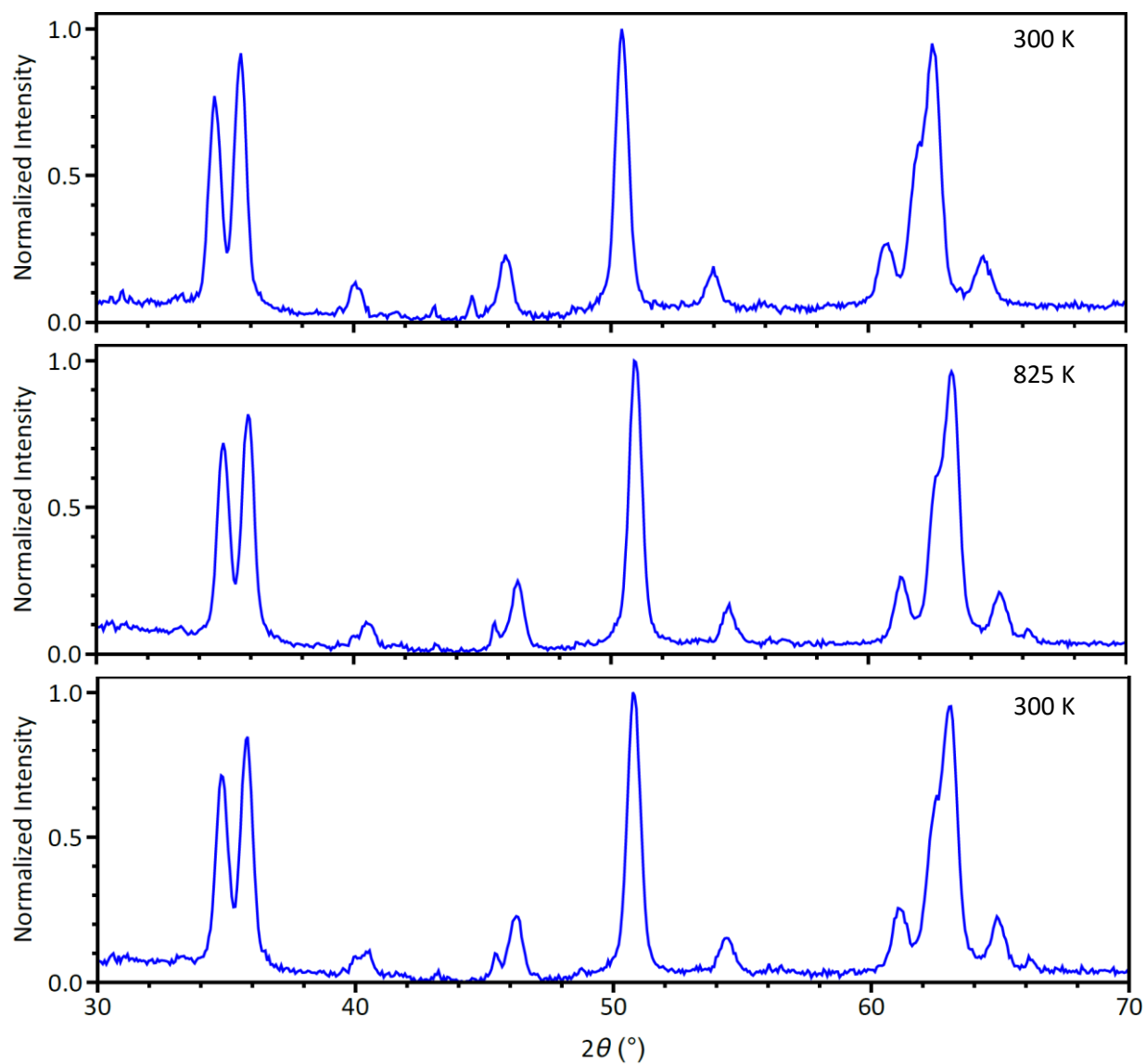
E *In situ* XRD NaYF₄ nanocrystals

Figure 21 *In situ* XRD diffractograms of NaYF₄ nanocrystals before heating, during heating, and after heating to 825 K (top, middle, and bottom, respectively).

F *In situ* XRD NaYF$_4$@SiO$_2$ nanocrystals

Figure 22 *In situ* XRD diffractograms of NaYF$_4$@SiO$_2$ nanocrystals before heating, during heating, and after heating to 825 K (top, middle, and bottom, respectively).